The Upper, Deep, Abyssal and Overturning Circulation in the Atlantic Ocean at 30°S in 2003 and 2011

Alonso Hernández-Guerra[1], Lynne D. Talley[2], José Luis Pelegrí[3], Pedro Vélez-Belchí[4], Molly O. Baringer[5], Alison M. Macdonald[6] and Elaine L. McDonagh[7]

[1] Unidad Océano y Clima, Instituto de Oceanografía y Cambio Global, IOCAG, Universidad de Las Palmas de Gran Canaria, ULPGC, Unidad Asociada ULPGC-CSIC, Canary Islands, Spain
[2] Scripps Institution of Oceanography, University of California, San Diego, La Jolla, California, USA
[3] Institut de Ciències del Mar, CSIC, Passeig Marítim de la Barceloneta 37-49, 08003 Barcelona, Spain
[4] Centro Oceanográfico de Canarias, Instituto Español de Oceanografía, Santa Cruz de Tenerife, Canary Islands, Spain
[5] NOAA/Atlantic Oceanographic and Meteorological Laboratory, Miami, Florida, USA
[6] Woods Hole Oceanographic Institution, Woods Hole, Massachusett, USA
[7] National Oceanography Centre, European Way, Southampton, United Kingdom

Abstract

Mass transports for the thermocline, intermediate, deep and abyssal layers in the Atlantic Ocean, at 30°S and for 2003 and 2011, have been estimated using data from GO-SHIP hydrographic transoceanic sections and applying three inverse models with different constraints. The uppermost layers comprise South Atlantic Central Water (SACW) and Antarctic Intermediate Water (AAIW), with a net northward transport in the range of 12.1-14.7 Sv in 2003 and 11.7-17.7 Sv in 2011, which can be considered as the northward returning limb of the Meridional Overturning Circulation (MOC). The western boundary Brazil Current transports twice as much SACW in 2003 (-20.2±0.7 Sv) than in 2011 (-9.7±0.7 Sv). A poleward current consisting of AAIW and Upper Circumpolar Deep Water (UCDW) flows beneath the Brazil Current. The eastern boundary Benguela Current, characterized by a high mesoscale eddy activity, transports 15.6±0.9 Sv in 2003 and 11.2±0.8 Sv in 2011, east of the Walvis Ridge. In the ocean interior, the northward flow is mainly located east of the Mid Atlantic Ridge (MAR) where Agulhas Rings (ARs), observed in both 2003 and 2011, transport warm and salty water from the Indian to the Atlantic Ocean. For the deep layers, the southward transport of North Atlantic Deep Water (NADW) occurs as the Deep Western Boundary Current and also in the eastern basin. The western and eastern basins transport similar amounts of NADW to the south during both years, although the eastern pathway changes substantially between both years. The total NADW transport, which is also considered the MOC, is in the range 16.3-24.5 Sv in 2003 and 17.1-29.6 Sv in 2011, hence with no significant change.

1. Introduction

During the 1990s, the international World Ocean Circulation Experiment (WOCE) surveyed all of the main ocean basins. The global network of high quality hydrographic data from transoceanic zonal and meridional sections of closely spaced stations allowed estimates of the oceanic transports of mass, heat, freshwater and other properties, from the sea surface to the bottom of every ocean (Ganachaud and Wunsch, 2003; 2000; Macdonald and Wunsch, 1996). The general features of the ocean's global overturning long predated WOCE (e.g. summaries in Gordon (1986) and Schmitz (1995)), but the newly collected global-scale data along with the newly-developed approach of inverse modeling allowed an improved, internally consistent, quantification of global transports (Roemmich and Wunsch, 1985; Wunsch, 1996). From these data, a clearer picture of the global circulation emerged, including a continued recognition of the pivotal role of the Atlantic Meridional Overturning Circulation (AMOC) (Ganachaud and Wunsch, 2003; 2000; Macdonald, 1998; Macdonald and Wunsch, 1996; Talley, 2013).

In the Atlantic Ocean, about 15 Sv of North Atlantic Deep Water (NADW) originate in the northern North Atlantic, essentially as Labrador Sea Water (Talley and McCartney, 1982) and overflow waters from the Nordic Sea (Smethie et al., 2000), and flow south mainly via a Deep Western Boundary Current (DWBC) (Fine and Molinari, 1988; Joyce et al., 2001; McCartney, 1993). During its transit to the Southern Ocean, the NADW entrains Antarctic Intermediate Water (AAIW) at its upper boundary and Antarctic Bottom Water (AABW) at its lower boundary (de Carvalho Ferreira and Kerr, 2017; Johnson, 2008), increasing to a southward mass transport of approximately -23 Sv at about 30°S. This southward mass transport of NADW has to be balanced by a northward flow of abyssal and thermocline waters, consisting of about 6 Sv of AABW and 17 Sv from the South Atlantic and Indian Oceans, the latter through the Agulhas leakage around the southern tip of Africa (Beal et al., 2011; Gordon, 1985a).This pattern of circulation has been summarized by Schmitz and McCartney (1993) for the North Atlantic circulation and Schmitz (1995), Talley (2008) and Talley (2013) for the global ocean circulation.

Following WOCE, a natural next step has been to estimate how the property transports and patterns of circulation have changed over time. For this purpose, repeat hydrographic sections in key latitudes and longitudes have been accomplished in the framework of the Global Ocean Ship-based Hydrographic Investigation Program (GO-SHIP) (www.go-ship.org). High accuracy measurements of different ocean properties – including temperature, salinity, nutrients and oxygen – are collected from the surface to the bottom of the ocean with an approximate decadal base and with the same horizontal sampling strategy as in WOCE, that is, a spatial resolution of 55 km near the internal Rossby radius, and with sections that extend (close) from coast to coast or enclose regions, that is, with closed mass budgets.

A now classical method used to estimate the ocean circulation and property transports from closed hydrographic sections is the inverse method (Wunsch, 1996; 1977). However, the results differ depending on the a priori variance specified within the inverse model, and on specific constraints and initial conditions imposed in the models. As a result, each separately calculated inverse estimate of transports from a given hydrographic section tends to be different. If we are to determine that the differences in the solution are due to the decadal changes in hydrographic data, and not due to the differences in the inverse models, the same a priori variance, same data types, and same approach to constraints should be specified for the inverse models. Using this consistent approach, Hernández-Guerra et al. (2014) and Hernández-Guerra and Talley (2016) estimated the changes in the ocean circulation and Meridional Overturning Circulation at 7.5°N and 24.5°N in the Atlantic Ocean during 1992-93 and 2010-11, and in the Indian and Pacific Oceans at 30°S in 2002-03 and 2009. In addition, Katsumata and Fukasawa (2011) applied an inverse model to the hydrographic data collected in the Indian, Pacific and Atlantic oceans at 30°S during the WOCE (1992-95) and repeated in 2003-04.

At 30°S in the South Atlantic Ocean, the boundary currents in the thermocline layers of the subtropical gyre are the Brazil and Benguela Currents. The Brazil Current is the narrow southward western boundary current (Müller et al., 1998; Zemba, 1991) and the Benguela Current is a broad eastern boundary current flowing north with intense mesoscale activity (Garzoli et al., 1996; Macdonald, 1993). In the ocean interior, the net mass transport is to the north though there are alternative northward/southward flows, including the distinctive Agulhas Rings (Goni et al., 1997; Gordon and Haxby, 1990) often found in this part of the ocean. In the deep NADW layers, the main flow takes place via the DWBC although southward transport also occurs in the eastern basin (Garzoli et al., 2015; Reid, 1989; van Sebille et al., 2012; Tamsitt et al., 2017; Zangenberg and Siedler, 1998). In abyssal layers, AABW flows to the north with a gradual latitudinal decrease in mass transport.

Our main goal here is to extend to the South Atlantic Ocean at 30°S our previous studies of the Indian and Pacific Oceans, and to estimate if the ocean circulation and the Atlantic Meridional Overturning Circulation has changed in different decades, analyzing the hydrographic data collected in 2003 and 2011. To accomplish our main goal, section 2 presents the data for the two years, 2003 and 2011, and the vertical sections of the different ocean properties, aimed at describing the main water masses present at 30°S (e.g. Chapter 9 of Talley et al. (2011)). Section 3 presents the geostrophic transport relative to initial reference level choices and describes the characteristics of our inverse box model. The final mass transports for both years, obtained after applying the inverse model, are presented in section 4, including our estimate of the AMOC and its variability. Section 5 describes the horizontal circulation focusing on the upper, deep and abyssal layers. We summarize the principal results in section 6.

2. Data, vertical sections and water masses

Hydrographic data collected in 2003 and 2011 over the entire water column at stations along section A10, nominally at 30°S in the South Atlantic Ocean, are available through the Carbon Hydrographic Data Office (CCHDO, http://cchdo.ucsd.edu) (Table 1). They were collected as part of the international Global Ocean Ship-Based Hydrographic Investigations Program (GO-SHIP) (Talley et al., 2016). The 2003 section was part of the circumpolar Japanese Beagle expedition (Katsumata and Fukasawa, 2011; Katsumata et al., 2013). The 2011 section was collected by US GO-SHIP. Tracks deviated from the indicated latitude mainly at the western and eastern boundaries, in order to angle the section perpendicular to the currents (Figure 1). The distances between stations were about 50 km, with smaller spacing across boundary currents and strong topographic slopes. At each station, temperature and salinity every two decibars was reported using a CTD as well as water samples for salinity, oxygen, silicate and other chemical tracers. For both cruises, a Lowered Acoustic Doppler Current Profiler (LADCP) – at 300 kHz and 150 kHz in 2003 and 2011, respectively – provided an absolute velocity profile at each station. As in Hernández-Guerra and Talley (2016), LADCP data are helpful to constrain the boundary currents in the inverse model.

The transatlantic section may be divided into western and eastern basins, separated by the Mid-Atlantic Ridge (MAR). The vertical distributions of potential temperature (ϑ), salinity, neutral density (γ^n, (Jackett and McDougall, 1997)), oxygen and silicate are shown for both cruises in Figures 2-6. The 2003 A10 sections were originally presented by Katsumata and Fukasawa (2011) . We use the sections to identify the vertical and density distribution of the existing water masses. With the double objective of selecting the reference level (used to integrate the thermal wind equation) and calculating the partial transports, a description of the different water masses follows, following well-known classifications (Talley et al., 2011), and similar to Katsumata and Fukasawa (2011) description.

The South Atlantic Central Water (SACW) extends from the surface to the density interface of γ^n=27.23 kg/m^3 (approximately 730 m depth), defining the thermocline layer. SACW is formed by subduction in the subtropical gyre of the South Atlantic Ocean, north of the subtropical front (Gordon, 1989; 1981; Sprintall and Tomczak, 1993). SACW is characterized by low silicate (<10 μM/kg) and high oxygen (>210 μM/kg), mainly in the shallowest thermocline layers (Figs. 5 and 6). According to Stramma and England (1999), SACW is transported to western Africa via the South Atlantic and Benguela Currents.

From an Optimum Multiparameter Analysis, Poole and Tomczak (1999) concluded that the eastern thermocline layers of the South Atlantic Ocean near 30°S also have a high contribution from the Indian Ocean, mainly in deeper layers (>500 m), due to the leakage of Indian Ocean thermocline waters through the Agulhas Retroflection (Gordon, 1985b; Poole and Tomczak, 1999; Sprintall and Tomczak, 1993). The relatively low-oxygen waters in the eastern basin around 3°E probably come from the Indian Ocean transported by the Benguela Current (Gordon et al., 1992). Another Indian Ocean contribution comes from the Agulhas Retroflection, as the Agulhas rings slowly propagate and diffuse out in the Atlantic Ocean (Casanova-Masjoan et al., 2017). Both cruises crossed one Agulhas ring: at about 1.5°E in 2003 and about 6.5°W in 2011, the former being stronger and deeper, reaching to the sea bottom, as shown by the downward dome of the isotherms and isopycnals (Figs. 2 and 4).

The signature of the Brazil and Benguela Currents is clear in the rising of the isotherms and isoneutrals near the western and eastern margins, respectively (Figs. 2 and 4). The Brazil Current stands as a relatively narrow poleward western boundary current while the Benguela Current appears as a relatively wide equatorward eastern boundary current, stretching westward to about 3°E (Garzoli et al., 1996). In the ocean interior, these isolines plunge slowly to the west, implying northward geostrophic flow relative to a reference layer located in deeper layers. The relatively low-oxygen waters near the eastern boundary represents tropical South Atlantic thermocline waters advected by an undercurrent at some 200 m depth (Gordon et al., 1995).

At intermediate levels (about $27.23\ kg/m^3 < \gamma^n < 27.58\ kg/m^3$, approximately in the 730-1140 depth range), the vertical section of salinity (Fig. 3) shows minimum values (<34.5) corresponding to Antarctic Intermediate Water (AAIW). The relative high oxygen in the western basin is accompanied by a salinity minimum. The sources of AAIW are primarily in the southeastern Pacific, in the northern Drake Passage and in the Malvinas Current loop (Suga and Talley, 1995). The northern limit of the minimum salinity corresponding to AAIW in the Atlantic Ocean is usually 20-25°N (Talley, 1996). At the western boundary, a relatively wide tongue of AAIW is transported through the Caribbean (Joyce et al., 2001). In the eastern basin, a narrow flow of AAIW has been repeatedly measured in the Lanzarote Passage, in the channel between the eastern Canary Islands and the African coast at ~29°N (Hernández-Guerra et al., 2017; Machín et al., 2010). The higher salinity in the eastern basin of the South Atlantic Ocean at any depth is due to the influence of older AAIW and mixed with Red Sea water entering from the Indian Ocean that contains higher salinity than the AAIW from the southwestern Atlantic Ocean (Shannon and Hunter, 1988). The decrease of oxygen in the eastern basin also points to origin in the Indian Ocean (Gordon et al., 1992; Talley, 1996). The patches of minimum salinity (<34.3) found in the western basin suggests that more recently ventilated AAIW is transported by northward flows in the ocean interior. Silicate increases with depth, at a maximum rate in the AAIW layer.

Below the AAIW, a body of oxygen-poor and relatively fresh water (core salinity of about 34.6) is observed corresponding to the Upper Circumpolar Deep Water (UCDW). The oxygen minimum occurs at the approximate density range between 27.58 kg/m^3 and 27.84 kg/m^3 (corresponding to approximately 1140-1560 m depth) (Figs. 4 and 5). The source of UCDW is located in the eastern South Pacific Ocean. It is transported to the western Atlantic margin through Drake Passage (Callahan, 1972) and transported to the eastern margin through an anticyclonic circulation as seen in (Reid, 1989). The UCDW stratum is thicker in the eastern than in the western basin, as also shown in Larqué et al. (1997).

The North Atlantic Deep Water (NADW) is best observed in the western basin but also stretches to the eastern basin, being transported by the Deep Western Boundary Current (Stommel et al., 1958) as a tongue of relatively high salinity (>34.85), high oxygen (>240 μM/kg) and low silicate (<50 μM/kg) (Figs. 3, 5 and 6). The NADW is composed of two different water masses formed at different locations: the Upper North Atlantic Deep Water (UNADW) essentially formed by Labrador Sea Water (Talley and McCartney, 1982) and the Lower North Atlantic Deep (LNADW) with overflow waters from the Nordic Sea (Pickart, 1992; Smethie et al., 2000). In the North Atlantic Ocean at 24.5°N, the UNADW is centered at about 2300 m and the LNADW is located at about 4000 m depth. Two lobes, one in each layer, of southward mass transport are observed centered at approximately these depths (Hernández-Guerra et al., 2014). By the time the NADW reaches 30°S, mixing has eroded the two-lobe signal, appearing as a single core in the density range 27.84-28.1 kg/m3 (from about 1600 to 3400 m), where single relative maximum of salinity and oxygen and a relative minimum in silicate are observed (Figs. 3, 5 and 6) (Tsuchiya et al., 1994). The NADW extends east, towards the MAR, with a decrease in salinity and an increase in silicate. According to Larqué et al. (1997), the relative minimum in silicate observed in the eastern basin is NADW. Thus, the southward flow of the NADW in the South Atlantic subtropical gyre occurs in both the western and eastern basins (Garzoli et al., 2015; Reid, 1989; van Sebille et al., 2012; Tamsitt et al., 2017), as will be discussed in Section 5.2. During its path to the south, the NADW splits the Circumpolar Deep Water into UCDW and Lower Circumpolar Deep Water (LCDW).

The densest water mass (γ^n>28.1 kg/m^3, from approximately 3420 m depth to the seafloor) is Antarctic Bottom Water (AABW), fresher with lower oxygen concentrations than the NADW (Fig. 3, 5). It is characterized by $\theta < 2$°C, $S < 34.86$ and silica concentration >70 μM/kg (Reid, 1989). The primary source of AABW at 30°S is LCDW (Heywood and King, 2002; Peterson and Whitworth, 1989; Reid et al., 1977), which is a mixture of Antarctic waters with NADW (de Carvalho Ferreira and Kerr, 2017; Mantyla and Reid, 1983). The westward shoaling of the near bottom isotherms and isoneutrals (γ^n=28.15 kg/m^3) indicates a northward AABW path, as shown by the highest silicate in the water column (Fig. 6). In the eastern basin, the Walvis Ridge prevents the equatorward flow of AABW.

3. Relative geostrophic transport and inverse model

The thermal wind equation is used to compute the relative geostrophic velocity normal to the vertical plane between two adjacent hydrographic stations. The relative geostrophic velocity depends on the selected reference layer, which is chosen near the the NADW-AABW interface, at γ^n=28.1 kg/m^3 (about 3420 m depth) (Fig. 4). This is the same reference layer used in a previous study carried out using the hydrographic data at 30°S in the Pacific and Indian Oceans (Hernández-Guerra and Talley, 2016). In their study of the oceanic fluxes in the South Atlantic, McDonagh and King (2005) used a similar reference layer for the A10 section carried out in 1993. However, our initial reference layer is slightly shallower than that used by Ganachaud and Wunsch (2000) and Ganachaud (2003) in their global transport study with the WOCE sections. In those station pairs where the deepest common depth is shallower than the reference layer, the bottom is considered as the reference layer; below the deepest common depth of each station pair, velocities are considered constant. The LADCP data can be used to estimate the velocity at the reference layer (Comas-Rodríguez et al., 2010; Joyce et al., 2001) and to constrain the mass transport in the boundary currents.

The mass and property transports have been computed for the different γ^n layers that divide the water column, selected following Talley (2008) and Hernández-Guerra and Talley (2016). When we require separate estimate of Ekman transports, which are introduced into the first layer, they have been computed from the NCEP wind stress (Kalnay et al., 1996) corresponding to the times of the cruises (Hernández-Guerra and Talley, 2016) (Table 2).

The initial mass transport through 30°S in the Atlantic Ocean is shown in Figure 7. The total mass transports present imbalances of 36.4 Sv for 2003 and 38.6 Sv for 2011, both northward as a result of thermocline and Antarctic Bottom Water transports, with almost no transport in the North Atlantic Deep Water layer, which is known from all previous analyses to have net southward transport. To reduce this large imbalance, we applied an inverse model to solve for an adjustment to the reference velocity reference velocity that seeks mass conservation (Wunsch, 1996; 1978). The following equation is solved:

$$\iint \rho b \, dx \, dz = -\iint \rho V_r \, dx \, dz + E_k \qquad (1)$$

where ρ is the density, b is the unknown reference velocity, V_r is the relative geostrophic velocity obtained from the thermal wind equation, E_k is the Ekman transport normal to the section, and (x, z) designate the along-section and vertical coordinates, respectively.

The above procedure would provide one single equation (vertically-integrated mass conservation) with 110 unknowns for 2003 and 119 unknowns for 2011 (the number of station pairs). New equations have to be introduced in order to reduce this underdetermined system. To be consistent with Hernández-Guerra and Talley (2016), when we later combine the results from those Indian and Pacific analyses with this Atlantic analysis, we apply several different inverse models using independent estimates as constraints for layer and total mass conservation (Table 3). Model A employs the mass transport and standard deviation from Talley (2008) (hereafter T08), obtained using the Reid (2003; 1994; 1997) absolute geostrophic analysis for transoceanic hydrographic sections carried out in 1959 and 1972 in the Atlantic Ocean at 32°S. Model B utilizes the mass transport and standard deviation from the Southern Ocean State Estimate (SOSE, http://sose.ucsd.edu) output for 2005-2007 (Mazloff et al., 2010), calculated from the zonally integrated flow at 30°S in neutral density layers. Our hydrographic data were collected in different years than T08's and SOSE's outputs. However, the standard deviation, used as a priori uncertainty in the inverse model, is large enough to allow the inverse model to adjust the mass transport for the oceanographic conditions of each cruise. Additionally, we set up model C as a 'classic' inverse model where, in addition to total mass conservation, we introduce several regional constraints. These local constraints are also used in models A and B.

Figure 8 shows the mass transports with standard deviations from T08 and SOSE that are then applied as constraints for inverse models A and B. The resemblance of the mass transport per layer for both transports is notable given their independence: the southward North Atlantic Deep Water (NADW) transport is compensated by northward bottom and surface water transports. T08 and SOSE differ in the abyssal layers: the transport is northwards in three layers in T08 while for SOSE there is only one layer transporting water northward, with the deepest layer showing no net flow. For the thermocline and intermediate layers, the northward mass transport is 12.8±2.3 Sv for T08 and 13.8±3.8 Sv for SOSE. The southward NADW transport is also not significantly different for T08 (-17.6±5.5 Sv) and SOSE (-16.1±4.2 Sv).

We introduce regional constraints for different longitude and depth ranges, listed in Table 4. The flow through the Bering Strait connects the Pacific and Atlantic Oceans with mean transports of -1.0±0.6 Sv and -1.2±0.6 Sv in models A and B, respectively, and -0.8±0.6 Sv in model C (Coachman and Aagaard, 1988); this constraint has been used in other inverse models (Ganachaud, 2003; Garabato et al., 2014; Macdonald, 1993). Constraints on the deep flow along the Vema Channel, as measured by Hogg et al. (1982) and Hogg and Owens (1999), and the deep flow through bathymetric constraints as in Walvis Ridge North and entering dead-end basins as the Walvis Ridge South (Ganachaud et al., 2000), are also applied to every model. The constraint of the total deep flow into the Brazil Basin comes from estimates by Hogg et al. (1999), Speer and Zenk (1993) and Zenk et al. (1999) in the western boundary over the Santos Plateau and the Vema and Hunter Channels. This constraint was also used by Saunders and King (1995) and Vanicek and Siedler (2002) in their inverse models. Similar deep constraints were considered by Rintoul (1991) in his study of the South Atlantic interbasin exchange. McDonagh and King (2005) used lower mass transports than ours as constraints for the Vema Channel and Brazil Basin.

We also constrain the relatively strong western and eastern boundary currents (Brazil and Benguela Currents) using LADCP data from the cruises. Stations with the same flow direction were selected to delineate the boundary currents. We could have used various previous transport estimates for these currents, as in McDonagh and King (2005) and Garabato et al. (2014). Both used an initial constraint of -25±10 Sv for the Brazil Current; the final adjusted solution after the inverse model was -11.4±1.6 Sv for Garabato et al. (2014) and -17.3±3.3 Sv for McDonagh and King (2005). Given this large difference between solutions and initial conditions, we have preferred to use the LADCP data from the cruises to initialize the field, as already done for the Agulhas Current in Hernández-Guerra and Talley (2016). Comas-Rodríguez et al. (2010) describe the procedure to adjust the geostrophy relative velocity to the LADCP-derived velocity profile from two adjacent stations. In order to reduce the high frequency, ageostrophic movements, we select the reference velocity by searching for a depth interval over which the vertical structure of the LADCP-derived velocity matches the relative geostrophic velocity.

Figure 9 shows four profiles of the LADCP-derived velocity, the geostrophic relative velocity and the geostrophic velocity adjusted to the LADCP-derived velocity for both the Brazil and the Benguela Currents. In the Benguela Current, the flow is constrained only using the easternmost stations, where the isoneutral slopes are large (Fig. 4). Table 4 shows the initial mass transport (with zero reference velocity), the LADCP-adjusted mass transport used as a constraint, and the final mass transport resulting from each inverse model. The western boundary (Brazil) current constraint in 2003 contains deeper layers (1 to 7) than in 2011 (1 to 5), where the flow has the same direction as in the thermocline layers (see sections 5.1.1 and 5.1.2). Contrary to other models (McDonagh and King, 2005), the recirculation of the Brazil Current is not imposed but rather is inferred from the inverse model.

The inverse models A and C also adjust the Ekman transport (Tables 2 and 3) as in Ganachaud (2003), Fraile-Nuez and Hernández-Guerra (2006), Macdonald et al. (2009) and Hernández-Guerra et al. (2010) . As already mentioned, the Ekman transport used in model C is computed from the NCEP wind stress at the time of each cruise (Kalnay et al., 1996). For model A, we use the Ekman transport computed in T08 (see Table 3). The Ekman transport in model B is included in the transport of the first layer and not as an independent transport (Mazloff et al., 2010).

The solution of the inverse model follows the approach first carried out in Joyce et al. (2001) and subsequently developed in Hernández-Guerra and Talley (2016) with some specific differences. The closed box for the inverse model is formed by the transatlantic 30°S section plus the transport in the Bering Strait. The full matrix equation and its derivation is provided in the Appendix.

The inverse problem is solved through the Gauss-Markov method (Wunsch, 1996). This method requires a priori variance for each equation and each solution. The a priori variance of each equation for models A and B comes from the standard deviation of the constraints (Table 3). The a priori variances for the regional constraints for all three models come from their standard deviations (Table 4) except for the boundary currents where we have assigned 5 Sv to account for the noise in the LADCP data. The a priori variance for the solution is (2 cm/s)^2 in the ocean interior and (4 cm/s)^2 in the eastern and western boundaries where strong shear is expected.

The velocities at the reference level for every inverse model and year are presented in Figure 10. The adjusted velocities are not significantly different from zero at most stations in the interior, as in previous inverse models (Ganachaud, 2003; Hernández-Guerra et al., 2014; Hernández-Guerra and Talley, 2016). Significant adjustments occur in station pairs located at the boundaries for models A and B. This pattern is even more pronounced for model C, which has significant boundary adjustments and very low reference velocities elsewhere, with and weaker mesoscale patterns than models A and B. The adjusted Ekman transport is -0.3±0.04 Sv for model C during both realizations (Table 2). The inverse model adjusts the Ekman transport in 2003 but leaves it invariant in 2011. Our adjusted Ekman transports are not significantly different from the Ekman transport of -0.6±1 Sv estimated in Ganachaud (1999) 's inverse model. Although several other studies do not provide uncertainties for the estimated Ekman transports, their values are in agreement with ours: Vanicek and Siedler (2002) and Holfort and Siedler (2001) estimated an Ekman transport of -0.4 Sv and -0.35 Sv, respectively, at 30°S. Model B is not allowed to adjust for the Ekman transport.

4. Final adjusted transport

Figure 11 shows the final mass transports per layer after application of the inverse models. The net initial mass transport imbalances using a reference level of γ^n=28.1 kg/m^3 (36.4 Sv for 2003 and 38.6 Sv for 2011) are greatly reduced and become indistinguishable from the transport in the Bering Strait, as seen from the total transports in Table 5: -1.04±2.62/-1.15±2.71 Sv in 2003/2011 for model A; -1.16±2.76/-1.24/2.95 Sv in 2003/2011 for model B; and -0.78±4.48/-0.79±4.97 Sv in 2003/2001 for model C.

Table 4 shows the constraints for specific layers and longitude ranges used in the inverse models, as well as the initial and final mass transports for each inverse model. These final mass transports satisfy the constraints within the uncertainty except for model B. This model does not meet the constraint in Vema Channel, Walvis Ridge North and eastern boundary (Benguela) current in 2011. Model A does not quite meet the Walvis Ridge North constraint in 2011.

4.1. Meridional transport per layer

Figure 11 and Table 5 show the meridional mass transports per neutral density layer for 2003 and 2011. Every model and year show the same pattern that is familiar from all previous analyses of the meridional overturning circulation at this latitude: northward flow corresponding to thermocline and intermediate layers, southward flow in the NADW deep layers, and northward flow in the AABW abyssal layers. Bottom/deep waters show the maximum northward/southward AABW/NADW transports in the same density layers: 28.15-28.23 kg/m^3 (3760-3840 m) and 27.84-28.04 kg/m^3 (1560-2600 m), respectively, with no significant differences between 2003 and 2011 for any model (Table 5). In contrast, for the thermocline layers, model C shows more northward transport in a shallower layer (26.14-26.45 kg/m^3, 120-240 m) than models A and B (26.45-27.0 kg/m^3, 240-560 m).

Whereas southward NADW transport in the North Atlantic is carried in two separate layers corresponding to the UNADW formed in the Labrador Sea and the LNADW of overflow waters, as seen at 24.5°N (Hernández-Guerra et al., 2014), these separate layers merge into a single layer by 30°S, spanning approximately the same density layers as at 24.5°N (Fig. 11). This coalescence of the UNADW and LNADW into a single NADW layer occurs around 25°S (Tsuchiya et al., 1994) and can be tracked using tracers such as oxygen and chlorofluorocarbons on the full set of zonal WHP vertical sections for the Atlantic (Koltermann et al., 2011).

Table 6 shows the integrated mass transport over the set of layers that flow in the same direction. The northward flow corresponding to the thermocline and intermediate layers lies in the range from the surface to 27.58 kg/m^3 (1140 m depth), which coincides with SACW and AAIW. The northward transport is in the range of 11.7-14.7 Sv in 2003 and 11.2-17.7 Sv in 2011, depending on the model. The northward transports for models A and B in 2003 and 2011 are not significantly different, taking into account their uncertainty. In contrast, model C presents a significant increase from 2003 (13.4±1.3 Sv) to 2011 (16.3±1.4 Sv). Figure 11 indicates that the net northward transport in the thermocline layers is higher than the transport in the intermediate layer. For example, for model C, the northward transport for SACW/AAIW is 12.3±1.0/1.2±0.9 Sv for 2003 and 15.3±1.1/1.0±0.9 Sv for 2011.

The deep (NADW) southward mass transport reaches down to γ^n=28.1 kg/m^3 (3420 m depth) in model A and deeper in models B and C (γ^n=28.15 kg/m^3, 3760 m depth) as seen in Figure 11. The deep transports for both years in all three models are nearly the same, within their uncertainty (Table 6). Model C presents the highest difference in mass transport between 2003 (-20.7±3.8) and 2011 (-25.4±4.2) but not significantly different.

The bottom (AABW) northward mass transport presents a similar value for 2003 in all three models, with a minimum transport of 4.1±1.1 Sv in model A and a maximum transport of 6.5±1.9 Sv in model C. Northward transports for models A and B are comparable and do not change between 2003 and 2011. In contrast, the AABW northward transport in model C in 2011 (8.3±2.1 Sv) is significantly different from the transports in models A and B (4.8±1.1 Sv and 3.6±1.6 Sv, respectively) although model C does not change significantly between 2003 and 2011.

4.2. Meridional Overturning Transport

The meridional overturning transport across 30°S for the Atlantic Ocean is computed by vertically integrating the mass transport from the bottom to the surface of the ocean (Fig. 12). The intensity of the overturning is often described as the maximum in the overturning stream function (zonally average transport integrated from the surface down), comprising northward flowing thermocline and intermediate waters, and southward flow in the deep layers (Kanzow et al., 2007; Koltermann et al., 2011) (Table 6). In our case, this layer is $\gamma^n<27.58$ kg/m^3 (1140 m), approximately similar to the overturning depth estimated by Garzoli et al. (2013) and Meinen et al. (2013) (1250 m and 1170 m, respectively) for 34.5°S and slightly deeper than the overturning depth (about 1100 m) at 24.5°N and 26°N (Cunningham et al., 2007; Hernández-Guerra et al., 2014). Models A and B show no significantly difference in the Atlantic Meridional Overturning Circulation (AMOC) in 2003 (13.3±0.9 for model A and 12.5±0.8 Sv for model B) and 2011 (12.5±0.8 Sv for model A and 12.0±0.8 Sv for model B). In contrast, model C shows a significant increase from 2003 (13.4±1.3 Sv) to 2011 (16.3±1.4 Sv).

Our estimates are lower than previous AMOC estimates carried out near 34.5°S from expendable bathythermograph (XBT) and WOA13 data, which are in the range 14.7-22.7 Sv (Garzoli et al., 2013). Dong et al. (2009) used XBT data from 2002 to 2007 to infer a time-mean AMOC of 17.9±2.2 Sv. Meinen et al. (2018), from about 6 years of pressure-inverted echo sounders (PIES) data at 34.5°S, estimated a mean AMOC transport of 14.7 Sv, closer to our results, with a relatively high standard deviation of 8.3 Sv. This high standard deviation and the large differences in the assessments suggest the AMOC experiences high variability. In this sense, Meinen et al. (2013) observed a very variable AMOC transport ranging from 3 to 39 Sv using 20 months of PIES data at 34.5°S. Dong et al. (2015) and Meinen et al. (2018) calculated substantial seasonal AMOC variability with the minimum from September to November, the time period when the cruises were carried out (Table 1).

Following Evans et al. (2017), the AMOC is also estimated as the southward flow of deep waters consisting primarily of NADW, or the converse, the northward flow of all waters that are not NADW. With this interpretation of the AMOC, the total northward flow (surface, thermocline, intermediate and abyssal waters) is considered. Table 6 shows a similar AMOC in 2003 in models A (-18.5±2.2 Sv) and B (-18.7±2.2 Sv), which are not significantly different in 2011 (-19.4±2.3 Sv in model A and -16.8±2.3 Sv in model B). Model C presents a lower AMOC in 2003 (-20.7±3.8) than in 2011 (-25.4±4.2 Sv) although not significantly different. Using a global inverse model, Ganachaud (1999) estimated an AMOC of deep waters of -23±3 Sv, consistent with our results. Other estimates are also consistent with our results: -21±2.8 Sv by Macdonald (1998), -22.7 Sv by Holfort and Siedler (2001), -19.9±2 Sv by McDonagh and King (2005) and 20±2 Sv by McDonagh and King (2005) and -17.6±5.5 Sv by Talley (2008).

5. Horizontal Circulation

The horizontal distribution of the meridional velocity through the transoceanic sections, calculated relative to γ^n=28.1 kg/m^3 (near 3300 m), is shown in Figure 13. Substantial variability is observed in the ocean interior, characterized by an alternating velocity sign. The velocity field shows relatively strong western and eastern boundary currents. In the western basin, the Brazil Current width is some 255 km and 145 km in 2003 and 2011, respectively, comparable with an offshore extension of some 200 km found by Müller et al. (1998); however, the depth of this baroclinic current is larger in 2003 than in 2011 (Figure 13). In both years, a major fraction of the Brazil Current recirculates in the western basin. In the eastern basin, there is high variability, associated with both the Benguela Current and the presence of an Agulhas ring at 1.5°W and 6.5°W in 2003 and 2011, respectively.

Figure 14 shows the mean Absolute Dynamic Topography (ADT) for November 2003 and September/October 2011, respectively, corresponding to the cruises carried out during these years, and the ADT for the western and eastern boundaries at the times when the hydrographic stations were done. Figure 15 shows the accumulated mass transport for the shallowest layer resulting from both the inverse models and the ADT. Both figures show the Brazil and the Benguela Currents and the equatorward ocean-interior flow, more pronounced in 2003. The inverse models and ADT match well in 2003; in contrast, in 2011 the Brazil and Benguela Currents show up more intense from the ADT than from the inverse models while the ocean interior flows are fairly similar.

Figure 16 shows the horizontal distribution of the meridional transport in isopycnal layers for every inverse model and year. This distribution is obtained by integrating the mass transport in layers with the same direction of flow as seen in Figure 11 by accumulating the transport eastward from zero at the western boundary. The uppermost layers have northward transport, the mid-depth layers experience southward transport, and the bottom layers again have northward transport (section 4.1). We next briefly discuss the flow and transport patterns as inferred from the velocity fields.

The A10 section at 30°S is right in the midst of the South Atlantic eddy field that is dominated by Agulhas Rings (ARs) (Figure 14). These rings originate in the Agulhas retroflection, move northwestward in the Cape Basin, and then westward across the Atlantic (e.g. Laxenaire et al., 2018). The Absolute Dynamic Topography (ADT) distributions in Figure 14 display relatively strong ARs in the eastern South Atlantic east of Walvis Ridge in 2003 and 2011, at 1°W and 6°W, respectively. Our transport analyses especially show the strong AR in 2003 that was directly sampled by A10. Weaker ARs are also observed east of the Walvis Ridge. ARs appear as an intermittent signal in the accumulated mass transport (Figure 16). Nevertheless, the net transport and the path of the Benguela Current is apparent in the accumulated mass transport.

5.1. Upper ocean circulation

The accumulated mass transport for the upper ocean, consisting of thermocline and intermediate waters (surface to γ^n=27.58 kg/m^3, about 1140 m depth), shows the usual subtropical gyre: a relative intense western boundary current flowing poleward, a northward recirculation east and close to the western boundary, and a northward transport in the ocean interior with a relative intense Benguela Current in the eastern boundary (Figure 16a). The pattern of circulation of thermocline and intermediate waters is similar to that shown in Stramma and England (1999). The patterns of the layer-integrated transports for models A and B do not change substantially between 2003 and 2011. In contrast, model C shows a slightly smaller accumulated transport, clearly seen between 40°W and 20°W.

5.1.1. Western Boundary current - Brazil Current

The Brazil Current transports SACW poleward in the surface and thermocline layers (γ^n<27.23 kg/m^3, down to 730 m) (Figs. 13, 16, 17) (Munk, 1950; Stommel, 1948). This is approximately the same depth range that Müller et al. (1998) found for the Brazil Current from current moorings installed near 28°S. Previous studies have shown that the transport of the Brazil Current increases towards the south due to a recirculation cell found in the western South Atlantic south of 28°S: from -10 Sv at 23°S-24°S to -17.5 Sv at 33°S (Stramma, 1989). Garzoli et al. (2013) also detected this increase in transport to the south, with even higher gradient transports: -8.6±4.1 Sv at 24°S and -21±4.7 Sv at 35°S.

Table 7 presents the Brazil Current mass transports in the surface and thermocline layers, as well as the transports in the AAIW and UCDW layers flowing beneath the Brazil Current: from the initial solution (layer of no motion at γ^n=28.1 kg/m^3), the LADCP-adjusted velocity, and the results from models A, B and C. The mass transport of the Brazil Current in 2003 ranges between -19.2 and -20.9 Sv for the three models, similar to the LADCP-adjusted mass transport but higher than the initial mass transport. The mass transport in 2011 for models A and C (-9.9±0.6 Sv and -9.7±0.7 Sv, respectively) differs from model B (-12.7±0.6 Sv). Other studies at this latitude have characterized a higher Brazil Current transport of -23.9 Sv (Talley et al., 2003). Hence our mass transports are consistent with a greatly fluctuating Brazil Current, in the range of -7 Sv to -26 Sv, as estimated by Müller et al. (1998) near 28°S from a current meter array. The transport carried south by the Brazil Current at this latitude is much lower than for other western boundaries as the Gulf Stream (Joyce et al., 2001) and the Agulhas Current (Hernández-Guerra and Talley, 2016), although some studies have shown it increasing quickly to greater than 70 Sv by 36°S (Peterson, 1992).

In 2003, a cyclonic eddy, detected from 44.8°W to 41.2°W, is embedded in the western-margin recirculation (Figure 16). This probably causes fairly different recirculations for each model: 6.0±0.9 Sv in model B, 9.7±0.9 Sv in model A and 12.7±1.2 Sv in model C. In 2011, the recirculation of the Brazil Current extends to 44.9°W, with higher mass transports: 13.1±0.7 Sv for model A, 13.4±0.7 Sv for model B and 11.9±0.7 Sv for model C.

At 30°S, a poleward intermediate current of AAIW (27.23 kg/m^3<γ^n<27.58 kg/m^3) and UCDW (27.58 kg/m^3<γ^n<27.84 kg/m^3) occurs under the Brazil Current (Hogg et al., 1999; Müller et al., 1998; Reid et al., 1977; Warner and Weiss, 1992). Our results show a relative strong/weak poleward transport of AAIW and UCDW in 2003/2011 (Figure 17, Table 7). The mass transport in 2003 ranges from -4.0 to -6.3 Sv for AAIW and -3.8 to -7.2 Sv for UCDW. In contrast, the mass transport in 2011 is much less for AAIW (-0.1 to -1.1 Sv) and not significantly different than zero for UCDW. These mass transports are consistent with previous results of Müller et al. (1998) that estimated a transport of -1.4 Sv for AAIW and -2.0 Sv for UCDW. Ganachaud (1999) in his global circulation inverse model estimated a mass transport of -14±4 Sv at 30°S for the Brazil Current but including the AAIW layer, approximately similar to our results for 2003.

5.1.2. Eastern Boundary current - Benguela Current

The Benguela Current is the broad eastern current of the South Atlantic Subtropical Gyre, analogous but more intense than the Canary Current in the North Atlantic Subtropical Gyre (Hernández-Guerra et al., 2005; Peterson and Stramma, 1991; Talley et al., 2011). The atmospheric conditions in the Benguela Current area are strongly influenced by the South Atlantic High over the subtropical South Atlantic, leading to southeasterly prevailing winds that induce offshore Ekman transport and cause coastal upwelling (Hernández-Guerra and Nykjaer, 1997; Nelson and Hutchings, 1983). In the South Atlantic, the upwelled cold waters are detected along the entire west coast of southern Africa (from about 18°S to the tip of Africa near 35°S) (Nelson and Hutchings, 1983). The Benguela upwelling system has seasonal behavior due to the meridional shift of the high pressure system. Along the southern/northern portion of the Benguela Current area the main upwelling occurs during the southern summer/winter (Weeks et al., 2006). Figure 2 shows that the surface isotherms in 2011 upwell towards the eastern coast such that isotherms warmer than 19°C outcrop; such upwelling was absent in 2003.

According to the sea surface dynamic topography, the Benguela Current is confined between the African coast and the Walvis Ridge (about 3°E) (Reid, 1989) . It is fed by both the South Atlantic Current, the southern boundary current of the South

Atlantic Subtropical Gyre, and Indian Ocean thermocline waters, detaching as rings and filaments from the Agulhas Current round the southern tip of Africa (Gordon et al., 1992; Stramma and Peterson, 1990). Clement and Gordon (1995), using ADCP-referenced geostrophic velocities, estimated a baroclinic northward Benguela Current transporting 25 Sv across 30°S in the upper kilometer. Similar transports were estimated by Fu (1981) from an inverse model and several other studies (Gordon et al., 1992; Stramma and Peterson, 1990; 1989). Garzoli et al. (2013) used 10 years of XBT data at 35°S to estimate the transport of the Benguela Current as 22.5±4.7 Sv.

Our estimates of mass transport in the surface and thermocline layers are lower than the above results. In 2003, the mass transport is 15.6±0.9 Sv from models A and C, and 15.4±0.9 Sv from model B (Table 8), and in 2011 it is even less, in the range of 10.4-12.9 Sv. Nonetheless, given the associated error bar, these estimates are comparable to the results shown in Garzoli et al. (1996) from PIES data. These authors suggested that the Benguela Current was composed of a stationary flow near the African coast (7.5°E -14.7°E), with a mean northward Benguela Current of 9.6 Sv for most of the observed period and a transient flow formed by large Agulhas rings shed from the Agulhas retroflection, injecting Indian subtropical thermocline water into the Benguela Current in the longitude range 3°E-7.5°E. The transport in this longitude range shows high variability, with a mean value of 3.2 Sv and even higher standard deviation that suggests occasional flow reversals. However, our results show high mesoscale eddy variability in the path of the entire Benguela Current, which shows up as a sawtooth-like streamfunction in the upper layers (Figure 16a). The eddy signal is noticeably observed west of about 12°E, with a clear northward flow east of this longitude (where we constrained the geostrophic velocity to the LADCP-derived velocities). These results show that the Benguela Current is stronger than the Canary Current and the Chile-Peru Current, its eastern boundary counterparts in the North Atlantic and South Pacific subtropical gyres (Hernández-Guerra et al., 2005; Hernández-Guerra and Talley, 2016).

Beneath the thermocline layer, the AAIW flows north similar to the Benguela Current while the deeper layers generally flow south (Reid, 1989). Table 8 shows fairly similar northward AAIW transports in 2003 and 2011. The mass transport differs in every model, presenting the lowest values in model C (1.9±0.9 Sv in 2003 and 1.0±0.8 Sv in 2011) and the highest numbers in model B (3.4±0.9 Sv in 2003 and 3.3±0.8 Sv in 2011).

5.1.3. Ocean Interior Circulation

For every model and year, the ocean interior presents a net equatorward flow. East of approximately 15°W, the three models show similar behavior in the interior gyre circulation both in 2003 and 2011. However, west of this longitude, the models display differences related to the recirculation of the Brazil Current (Fig. 16a). The streamfunctions for model C in 2003 and 2011 are flatter than for models A and B. In 2003, the streamfunction in every model presents an approximate constant positive slope through the ocean interior east of the recirculation of the Brazil Current. In contrast, the streamfunction in 2011 shows a relatively large southward flow from the end of the recirculation to ~39.8°W (corresponding to the Santos Plateau) with different mass transport in each model.

In 2011, models A and B present relatively large mass transports (-18.7±1.6 Sv and -23.6±1.5 Sv) and model C displays a much lower value (-9.6±1.8 Sv). In the Brazil Basin (39.8°-19.0°W) there is weak southward mass transport in models A and C (-4.4±2.4 Sv and -3.4±2.7 Sv) and no significant flow in model B (-0.6±2.4 Sv). Thus, the equatorward flow of the South Atlantic subtropical gyre is located east of the MAR, with a mass transport of 32.0±2.3 Sv in model A, 34.0±2.3 Sv in model B, and 26.3±2.3 Sv in model C. From the boundary of the Brazil Current to the eastern boundary, the mass transport range is 35.9-40.5 Sv in 2003 and 22.9-28.1 Sv in 2011.

The hydrographic data collected in 2003 and 2011 show an Agulhas ring (AR), a warm and salty anticyclonic eddy containing water of Indian Ocean origin, centered at about 1.5°W and 6.5°W, respectively (Figs. 2-4). The ARs are eddies shed by the Agulhas Current Retroflection, which is a tight loop formed when the southward Agulhas Current encounters the eastward South Atlantic and the Antarctic Circumpolar Currents (Feron and De Ruijter, 1992). The ARs retain their Agulhas Current characteristics (warmer and saltier than the surrounding South Atlantic surface water) for several years (usually 2-4 years) until their decay (Goni et al., 1997; Richardson, 2007). The ARs observed in 2003 and 2011 are both about 400 km in diameter; however, their vertical extension (illustrated by the downward dome of the isotherms and isopycnals) is quite different, with the 2003 AR extending from the sea surface down to 4500 m but the 2011 AR only reaching to 1500 m (Figures 2 and 4). In 2003, the deep AR in all models has large rotating geostrophic mass transport in the thermocline and intermediate layers (layers 1-5, $\gamma^n<27.58$ kg/m^3), in the range of 57.2-61.9 Sv. In deeper layers, the signal of the AR is not observed in models A and B. In contrast, model C yields a rotating mass transport of 13.2±2.3 Sv in layers 6-7 (27.58 kg/m$^3<\gamma^n<28.04$ kg/m^3). In 2011, the rotating mass transport associated with the AR is smaller than for the 2003 AR, in the range of 26.6-35 Sv from the surface to $\gamma^n<27.84$ kg/m^3 (layer 6).

5.2. Deep ocean circulation

Figure 16b shows the accumulated mass transport for the NADW layers, considered as those deep layers that flow south: layers 6 to 8 in model A and layers 6 and 9 in models B and C. The streamfunction for model A resembles the streamfunction for model B for each year separately. In contrast, the streamfunction for model C behaves differently although the net mass transport in each model is similar (Table 6). The net southward mass transport of NADW through 30°S in 2003 is similar for model A (-18.5±2.2 Sv) and model B (-18.7±2.2) and slightly higher in model C (-20.7±3.8). In 2011, the NADW transport is also not significantly different in models A (-19.4±2.3 Sv) and B (-16.8±2.3 Sv), while model C presents a higher mass transport (-25.4±4.2 Sv).

Many different studies have concluded that the NADW is transported southwards mainly by the DWBC in the Atlantic Ocean (Ganachaud, 2003; Meinen and Garzoli, 2014; Meinen et al., 2017; Müller et al., 1998). As shown in Figure 16b and Table 9, a relatively strong recirculating DWBC is observed in all models except for model C in 2011. In 2003/2011, the DWBC extends to approximately 39.8°/39.1°W. Model B shows a significantly different transport between 2003 (-35.3±3.4 Sv) and 2011 (-44.4±3.7 Sv). Model A also shows a relatively strong southward DWBC, transporting -27.5±4.0 Sv in 2003 and -30.2±3.8 Sv in 2011. In contrast, model C shows a relatively weak DWBC in 2003 (-16.1±5.1 Sv) and absent in 2011 (Table 9).

The recirculation of the DWBC extends to about 38.2°W in 2003 and to 37.8°W in 2011 (Table 9). The northward mass transport of the recirculation of the DWBC is lower in 2003 (9.8±1.4 Sv in model A and 10.9±1.3 Sv in model B) than in 2011 (14.9±1.6 Sv in model A and 23.5±1.6 Sv in model B). Model C presents a recirculation in 2003 with a mass transport (8.4±1.1 Sv) not significantly different from models A and B, but shows no recirculation in 2011.

East of the DWBC recirculation, model C in 2003 and in 2011 presents an approximate linear southward mass transport in the entire ocean interior. In contrast, models A and B present northward and southward flow at different longitude ranges. Models A and B in 2003 and in 2011 present a flat streamfunction over approximately the Rio Grande Rise with no significant mass transport (1.3±3.7/-3.4±3.9 Sv and 1.6±4.0/-3.9±4.0 Sv in 2003/2011 for models A and B, respectively). A deep anticyclonic eddy is detected over the Brazil Basin with a very strong mass transport in 2011 (-20.3±3.7 Sv in model A and -18.1±4.0 Sv in model B). Every model describes a northward flow in the range of 4.5-15.0 Sv and 9.1-21-6 Sv in 2003 and 2011, respectively, on the western flank of the MAR, and a mass transport not significantly different than zero over the MAR (-2.3±5.0/2.6±4.4 Sv for models A/B in 2003 and -1.1±4.5/2.2±4.5 Sv for models A/B in 2011). Thus, west of the MAR, the net southward transport is not significantly different in every model and year, with a transport of -8.5±4.6/-3.0±4.7 Sv in model A/B in 2003 and -7.1±4.8/-5.7±4.9 Sv in model A/B in 2011 as shown in Table 10. East of the MAR, we find a similar southward mass transport in 2003 and 2011 (-10.0±4.6/-15.6±4.6 Sv for models A/B in 2003 and -12.3±4.7/-11.1±4.8 for models A/B in 2011). The zonal extension of the southward mass transport east of the MAR is narrower in 2003 (from 1°E, east of Walvis Ridge, to the eastern boundary) than in 2011 (from the MAR to the eastern boundary). Table 10 also shows that model C provides similar mass transport west (-12.5±5.5 Sv in 2003 and -12.8±5.5 Sv in 2011) and east (-8.2±5.6 Sv in 2003 and -12.7±5.5 Sv in 2011) of the MAR. Southward mass transports east of the MAR are similar to the estimations provided by Arhan et al. (2003). Curiously, the mesoscale patterns in 2003 mirror those in 2011: a cyclonic eddy over the Angola Basin in 2003 is an anticyclonic eddy in 2011, similarly with the two eddies over the Cape Basin.

5.3. Abyssal ocean circulation

In the western basin, the path of the Antarctic Bottom Water (AABW) is constrained by the shoals of the Rio Grande Rise that define the separation between the Brazil Basin and the Argentina Basin. The northward path of the AABW is through the deepest layers over the Santos Plateau (Speer and Zenk, 1993), the Vema Channel (Hogg et al., 1982) and the Hunter Channel (Speer et al., 1992) (Figure 1). In the eastern basin, we have constrained the model to have no flow through the Walvis Ridge (Warren and Speer, 1991) (Table 4).

Figure 16c presents the accumulated mass transport for the AABW layers. The mass transport for layers 9 to 11 in model A and layers 10 and 11 in models B and C shows northward flow (Figure 11) and, therefore, these layers are considered as the bottom layers for each model. The net abyssal northward transport is shown in Table 6. Model C presents the highest AABW transport in 2003 (6.5±1.9 Sv) and in 2011 (8.3±2.1 Sv) compared to the mass transport in model A (4.1±1.1 Sv in 2003 and 4.8±1.1 Sv in 2011) and model B (5.0±1.5 Sv in 2003 and 3.6±1.6 Sv in 2011).

Over the Santos Plateau, models A and B provide net southward mass transports of -2.5±0.9 Sv and -3.6±0.7 Sv, respectively, in 2003, and -2.7±1.1 Sv and -3.4±1.0 Sv, respectively, in 2011. In contrast, the mass transport in model C is northward with 0.4±1.1 Sv in 2003 and 2.5±1.1 Sv in 2011. Results from model C are in agreement with previous studies of the flow of AABW over the Santos Plateau that estimated a northward transport between 0.1 and 2 Sv (McDonagh et al., 2002; Speer and Zenk, 1993).

The northward transport through the Vema Channel is used as a constraint in the inverse models and the results of the mass transport from the three models have been adjusted accordingly (Table 4). However, the net mass transport just east of the Vema Channel is different in each model: models A/C present a northward mass transport of 1.2±1.0 Sv/3.4±1.1 Sv in 2003 and 0.8±1.1/6.1±1.2 Sv in 2011; in contrast, model B has a southward mass transport of -1.0±0.7 Sv in 2003 and -1.6±0.9 Sv in 2011 (Figure 16c).

West of the Vema Channel, every model adjusts the net northward mass transport to the constraint used in the Brazil Basin (Table 4). Models A and B show a marked anticyclonic circulation in the Brazil Basin between Rio Grande Rise and the MAR (28-19.5°W) in both years, and in both the deepest and the intermediate layers (Fig. 16). This feature does not occur in the smoothed circulation maps of Reid (1989), but it is also not a strong feature of our model C. Model A presents a cyclonic/anticyclonic eddy in 2003/2011 over the Angola Basin (7-1°W). The anticyclonic eddy in 2011 is a feature from the surface layers to the bottom of the ocean and associated with the Agulhas Ring with the bottom part presumably trapped by the topography. Over the Cape Basin (2.5-12°E), which is well known for strong mesoscale variability (e.g., Richardson (2007)), mesoscale patterns are observed in all models.

6. Concluding remarks

Three inverse models with different constraints have been applied to the zonal sections carried out at 30°S in the South Atlantic subtropical gyre. Model A constrains the mass transport per layer with the transports provided by Talley (2008), who uses the reference velocities adjusted from Reid (1994). Model B constrains the mass transport per layer using the transports estimates from the Southern Ocean State Estimate (SOSE) (Mazloff et al., 2010). The SOSE transports and standard deviation were zonally integrated in our neutral density layers from the 5-day archived SOSE output. Model C constrains the mass transport in a classical way, only using previous measurements carried out at different longitude and depth ranges (e.g., Ganachaud (2003), Lumpkin and Speer (2007) and Macdonald (1993)). These regional constraints have been also used in models A and B. Therefore, model C has greater freedom to find a solution. The three inverse models have been applied to the hydrographic sections carried out in 2003 and 2011, thus the differences in ocean circulation patterns reflect actual changes in the hydrographic data.

Although the similarity of the northward mass transport per layer for T08 and SOSE is remarkable for the thermocline and AAIW layers (Figure 8), the solution is substantially different for the deep and bottom layers, from the UCDW to the seafloor. The most noteworthy difference is at the abyssal AABW layers: T08 provides a net mass transport of 3.9±1.3 Sv while SOSE accounts for only 1.1±3.0, with zero mass transport in the bottommost layer. This is the main difference arising for the distinct set of constraints imposed in models A and B and it is also the reason why the adjusted mass transport using the SOSE constraints presents outliers and does not quite meet the different constraints in 2011. For example, results of the inverse model for layer 5 shown in Table 5 provide an AAIW transport not significantly different for models A and C. However, model B provides a transport significantly different from models A and C. This difference also occurs in layer 6 corresponding to UCDW. Thus, results from model B are not considered it in the following summary.

Net mass transports in the thermocline, intermediate, deep and abyssal layers are roughly similar to those obtained by Ganachaud (2003) from a global inverse model using the WOCE sections. These authors estimated a mass transport of 17.4±3.2 Sv, including the Ekman transport for the northward surface flow. Our results for the AMOC at 30°S are 12.1-14.7 Sv in 2003 and 11.7-17.7 Sv in 2011. For the NADW southward flow, the calculated mass transports are -16.3-24.5 Sv in 2003 and -17.1-29.6 Sv in 2011, which are not significantly different than the -23±3 Sv estimated by Ganachaud (2003). Northward mass transports estimated in different models and years for the bottom layers (3.0-8.4 Sv in 2003 and 3.7-10.4 Sv in 2011) are not significantly different from the 6±1.3 Sv estimated by Ganachaud (2003).

The pattern of circulation in the thermocline and intermediate layers of all our models agrees with those proposed by Stramma and England (1999): a relatively narrow western boundary Brazil Current flowing south, a continuous flow to the north in the ocean interior following the model of Sverdrup (Sverdrup, 1947) and a fairly broad Benguela Current in the eastern basin.

Our estimates indicate that the net northward thermocline transport is over 10 times the northward transport in the intermediate layers (Table 5). This result indicates that the thermocline transport dominates the return flow to the north, contrary to Ganachaud (2003) and Talley (2008; 2003), who estimated a more balanced partition between the thermocline and AAIW, and las Heras and Schlitzer

(1999) who suggested the total transport to be largely controlled by the intermediate water flow.

The deep circulation shows a relative strong DWBC in model A (-27.5±4.0 Sv in 2003 and -30.2±3.8 Sv in 2011) and a weaker DWBC in model C (-16.1±5.1 Sv in 2003 and absent in 2011). This different DWBC transports are consistent with the high variability estimated previously with in situ measurements: Meinen et al. (2017) used about 6 years of PIES data and showed a DWBC with a mean absolute geostrophic transport of -15 Sv with a higher standard deviation of 23 Sv. Just east of the DWBC, a northward recirculation is present in model A in 2003 and 2011 (9.8±1.4 Sv and 14.9±1.6 Sv, respectively) and model C in 2003 (8.4±1.1 Sv).

In the deep layers, the circulation shown in model A is very similar to the circulation maps at the NADW level shown by Reid (1989): a fraction of the relatively strong DWBC transporting mass transport to the south turns equatorward in the western basin and flows back to the south in the eastern basin eventually to leave the South Atlantic into the Indian Ocean (Speer et al., 1995). This scheme of circulation was also proposed by Hogg and Thurnherr (2005) and Zangenberg and Siedler (1998). In contrast, our model C shows a southward flow in the western and eastern basins that resembles the pattern of circulation of Stramma and England (1999) . These authors show that the NADW circulation in the western basin is separated from the eastern basin circulation, which is fed by the northernmost branch that detaches from the DWBC at about 20°S (Vanicek and Siedler, 2002). As the scheme of circulation in models A and C resemble the plots of Reid (1989) and Stramma and England (1999), respectively, we cannot conclude which is the preferred. Our results show similar southward transports west of the MAR (-8.5±4.6/-12.5±5.5 Sv in models A/C in 2003 and -7.1±4.8/-12.8±5.5 in models A/C in 2011) as east of the MAR (-10.0±4.6/-8.2±5.6 Sv in models A/C in 2003 and -12.3±4.7/-12.7±5.5 Sv in models A/C in 2011). The path of the eastern flow is highly variable: from about 1°E, east of Walvis Ridge, to the eastern boundary in 2003 and from the MAR to the eastern boundary in 2011.

In conclusion, the ocean circulation in the surface and thermocline, intermediate and abyssal layers and, therefore, the Atlantic Meridional Overturning

Circulation (AMOC) is not significantly different between 2003 and 2011 at 30°S in the South Atlantic, and is approximately similar to the 1990's ocean circulation.

The meridional circulation of the upper, deep and abyssal layers at 30°S in the Atlantic Ocean has been described in this paper. Hence, this study complements early efforts by Hernández-Guerra and Talley (2016), who determined the meridional circulation at 30°S in the Pacific and Indian Oceans in 2002-2003 and 2009. A circumpolar analysis, currently under progress, will naturally emerge as we stretch the 30°S section for all three oceans; these forthcoming analyses will include the heat and freshwater transports as well as a comparison with the WOCE sections.

Appendix.

The absolute geostrophic velocity (v_a) for a given station pair, as a function of depth (z), is the sum of a relative velocity (v) and the velocity, b, at the reference level:

$$v_a(z)=v(z) + b$$

The inverse model finds the optimal solution for b for each station pair that minimizes the variance according to the Gauss-Markov method. First, we apply mass conservation for the entire water column:

$$\iint \rho v_a dS = 0$$
$$\iint \rho(v + b)dS = 0 \qquad (A.1a,b,c)$$

And using discrete variables:

$$\sum_{j=1}^{N}\sum_{q=1}^{Q}\rho_{jq}(v_{jq} + b_j)a_{jq} = 0$$

where the area integral dS is over the entire area of the section, and a_{jq} is for each station pair j and isopycnal layer q. In A.1 and subsequent equations, the term $\rho_{jq}v_{jq}$ is first summed over each 2 dbar interval within layer q. (For silicate conservation, we multiply these equations with the silicate concentration but further steps are the same.) When mass transport is constrained to a particular non-zero value, for instance, the Brazil or

Benguela Currents, (A.1c) becomes:

$$\sum_{j=1}^{N}\sum_{q=1}^{Q}\rho_{jq}(v_{jq}+b_j)a_{jq}=M_{Total} \qquad (A.1d)$$

where M_{Total} is the total transport for the constraint, and the limits for station pairs and layers are related to the constraint. Due to noise from eddies, internal waves, aliasing, measurements errors, etc., total mass conservation is not exact:

$$\sum_{j=1}^{N}\sum_{q=1}^{Q}\rho_{jq}b_j a_{jq}+n_{Total}=-\sum_{j=1}^{N}\sum_{q=1}^{Q}\rho_{jq}v_{jq}a_{jq}+M_{Total} \qquad (A.2)$$

where n_{Total} is the noise.

Considering mass conservation in each layer q, we have the following equations:

$$\sum_{j=1}^{N}\rho_{jq}b_j a_{jq}+n_q=-\sum_{j=1}^{N}\rho_{jq}v_{jq}a_{jq}+M_q \quad q=1,2,\ldots,Q \qquad (A.3)$$

where M_q is the layer transport constraint and n_q is the layer noise. This is rewritten as

$$\sum_{j=1}^{N}e_{jq}b_j+n_q=y_q \qquad q=1,2,\ldots,Q \qquad (A.4)$$

where

$$e_{jq}=\rho_{jq}a_{jq}$$

$$y_q=\sum_{j=1}^{N}\rho_{jq}v_{jq}a_{jq}-M_q \qquad (A.5)$$

For silicate constraints, the e_{jq} elements are multiplied by silicate concentration at each point in the layer. We can then write the matrix equation (1):

$$\mathbf{Ab} + \mathbf{n} = -\mathbf{Y} \qquad \text{(A.6)}$$

where *b* is an *Nx1* vector of the unknowns (reference velocities), *A* is a *(Q+1) x N* matrix, *n* is a *(Q+1)x1* vector, and *Y* is a *(Q+1)x1* vector of values calculated from the CTD data and externally imposed mass transports. (Q is for the equations for each layer and the +1 is the equation for conservation of the whole water column.)

Next, the Ekman transport is included in the first layer and the total. We allow the inverse model to adjust the Ekman transport to the specific conditions of the cruise and the full matrix is:

$$\begin{pmatrix} e_{11} & \cdots & e_{1n} & 1 \\ e_{21} & & e_{2n} & 0 \\ \vdots & \ddots & \vdots & \vdots \\ e_{q,1} & & e_{q,n} & 0 \\ e_{q+1,1} & \cdots & e_{q+1,n} & 1 \end{pmatrix} \begin{pmatrix} b_1 \\ \vdots \\ b_n \\ \Delta T_{EK} \end{pmatrix} = \begin{pmatrix} y_1 + T_{EK} \\ y_2 \\ \vdots \\ y_q \\ y_{q+1} + T_{EK} \end{pmatrix} \qquad (A.8)$$

The Gauss-Markov estimator is applied to solve this matrix (Wunsch, 1996).

Acknowledgments

This study has been performed as part of projects: US CLIVAR Repeat Hydrography Program, which is now part of the International GO-SHIP project, with US funding from the US National Oceanic and Atmospheric Administration (NOAA) Climate Program Office, and National Science Foundation Geoscience Division, BOUNDARY (ProID2017010083) funded by RIS-3, PO Feder Canarias, VA-DE-RETRO (CTM2014-56987-P) and SAGA (RTI2018-100844-B-C31) funded by the Spanish government. This article is a publication of the Unidad Océano y Clima of the Universidad de Las Palmas de Gran Canaria, a R&D&i CSIC-associate unit. EM was supported by NERC national capability funding through the ORCHESTRA (NE/N018095/1) and CLASS (NE/R015953/1) projects. The wind data were collected from NCEP Reanalysis Derived data (http://www.esrl.noaa.gov/psd/). Hydrographic data were collected from the CCHDO website (https://cchdo.ucsd.edu/). We thank to the chief scientists and teams from Japan and USA that collected these transect data: Y. Yoshikawa, M. Baringer (co-author) and A. Macdonald (co-author). The LADCP data were collected from Clivar/CO2 Repeat Hydrography Shipboard ADCP data program (http://currents.soest.hawaii.edu/clivar/ladcp). We also gratefully acknowledge M. Mazloff for the Southern Ocean State Estimate transports, and the late J.L. Reid for the historical Atlantic Ocean velocity analyses.

References

Arhan, M., Mercier, H., Park, Y.-H., 2003. On the deep water circulation of the eastern South Atlantic Ocean. Deep-Sea Res Pt I 50, 889–916. doi:10.1016/S0967-0637(03)00072-4

Beal, L.M., De Ruijter, W.P.M., Biastoch, A., Zahn, R., Cronin, M., Hermes, J., Lutjeharms, J., Quartly, G., Tozuka, T., Baker-Yeboah, S., Bornman, T., Cipollini, P., Dijkstra, H., Hall, I., Park, W., Peeters, F., Penven, P., Ridderinkhof, H., Zinke, J., 2011. On the role of the Agulhas system in ocean circulation and climate. Nature 472, 429–436. doi:10.1038/nature09983

Callahan, J.E., 1972. The structure and circulation of Deep Water in the Antarctic. Deep Sea Research 19, 563–575. https://doi.org/10.1016/0011-7471(72)90040-X

Casanova-Masjoan, M., Pelegrí, J.L., Sangra, P., Martínez, A., Grisolía-Santos, D., Pérez-Hernández, M.D., Hernández-Guerra, A., 2017. Characteristics and evolution of an Agulhas ring. J Geophys Res-Oceans 122. doi:10.1002/2017JC012969

Clement, A.C., Gordo, A.L., 1995. The absolute velocity field of Agulhas eddies and the Benguela Current. Journal of Geophysical Research 100, 22591–22601.

Coachman, L.K., Aagaard, K., 1988. Transports Through Bering Strait: Annual and Interannual Variability. Journal of Geophysical Research 93, 15535–15539. doi:10.1029/JC093iC12p15535

Comas-Rodríguez, I., Hernández-Guerra, A., McDonagh, E.L., 2010. Referencing geostrophic velocities using ADCP data at 24.5°N (North Atlantic). Sci. Mar. 74, 331–338. doi:10.3989/scimar.2010.74n2331

Cunningham, S.A., Kanzow, T., Rayner, D., Baringer, M.O., Johns, W.E., Marotzke, J., Longworth, H.R., Grant, E.M., Hirschi, J.J.M., Beal, L.M., Meinen, C.S., Bryden, H.L., 2007. Temporal Variability of the Atlantic Meridional Overturning Circulation at 26.5°N. Science 317, 935–938. doi:10.1126/science.1141304

de Carvalho Ferreira, M.L., Kerr, R., 2017. Source water distribution and quantification of North Atlantic Deep Water and Antarctic Bottom Water in the Atlantic Ocean. Prog Oceanogr 153, 66–83. doi:10.1016/j.pocean.2017.04.003

Dong, S., Garzoli, S., Baringer, M., Meinen, C., Goni, G., 2009. Interannual variations in the Atlantic meridional overturning circulation and its relationship with the net northward heat transport in the South Atlantic. Geophysical Research Letters 36, L20606. doi:10.1029/2009GL039356

Dong, S., Goni, G., Bringas, F., 2015. Temporal variability of the South Atlantic Meridional Overturning Circulation between 20°S and 35°S. Geophysical Research Letters 42, 7655–7662. doi:10.1002/2015GL065603

Evans, G.R., McDonagh, E.L., King, B.A., Bryden, H.L., Bakker, D.C.E., Brown, P.J., Schuster, U., Speer, K.G., van Heuven, S.M.A.C., 2017. South Atlantic interbasin exchanges of mass, heat, salt and anthropogenic carbon. Prog Oceanogr 151, 62–82. doi:10.1016/j.pocean.2016.11.005

Feron, R.C.V., De Ruijter, W.P.M., 1992. Ring shedding in the Agulhas Current System. Journal of Geophysical Research 97, 9467–9477.

Fine, R.A., Molinari, R.L., 1988. A continuous deep western boundary current between Abaco (26.5N) and Barbados (13N). Deep-Sea Res 35, 1441–1450.

Fraile-Nuez, E., Hernández-Guerra, A., 2006. Wind-driven circulation for the eastern North Atlantic Subtropical Gyre from Argo data. Geophysical Research Letters 33. doi:10.1029/2005GL025122

Fu, L., 1981. The general circulation and meridional heat transport of the subtropical South Atlantic determined by inverse methods. J. Phys. Oceanogr. 11, 1171–1193.

Ganachaud, A., 2003. Large-scale mass transports, water mass formation, and diffusivities estimated from World Ocean Circulation Experiment (WOCE) hydrographic data. Journal of Geophysical Research 108, 3213. doi:10.1029/2002JC001565

Ganachaud, A., Wunsch, C., 2003. Large-scale ocean heat and freshwater transports during the World Ocean Circulation Experiment. Journal of Climate 16, 696–705.

Ganachaud, A., Wunsch, C., 2000. Improved estimates of global ocean circulation, heat transport and mixing from hydrographic data. Nature 408, 453–457.

Ganachaud, A., Wunsch, C., Marotzke, J., Toole, J., 2000. Meridional overturning and large-scale circulation of the Indian Ocean. J Geophys Res-Oceans 105, 26117–26134.

Ganachaud, A.S., 1999. Large scale oceanic circulation and fluxes of freshwater, heat, nutrients and oxygen. Massachusetts Institute of Technology and Woods Hole Oceanographic Institution, Woods Hole, MA. doi:10.1575/1912/4130

Garabato, A.C.N., Williams, A.P., Bacon, S., 2014. The three-dimensional overturning circulation of the Southern Ocean during the WOCE era. Prog Oceanogr 120, 41–78. doi:10.1016/j.pocean.2013.07.018

Garzoli, S.L., Baringer, M.O., Dong, S., Perez, R.C., Yao, Q., 2013. South Atlantic meridional fluxes. Deep-Sea Research I 71, 21–32. doi:10.1016/j.dsr.2012.09.003

Garzoli, S.L., Dong, S., Fine, R., Meinen, C.S., Perez, R.C., Schmid, C., van Sebille, E., Yao, Q., 2015. The fate of the Deep Western Boundary Current in the South Atlantic. Deep-Sea Research I 103, 125–136. doi:10.1016/j.dsr.2015.05.008

Garzoli, S.L., Gordon, A.L., Kamenkovich, V., Pillsbury, D., Duncombe-Rae, C., 1996. Variability and sources of the southeastern Atlantic circulation. Journal of Marine Research 54, 1039–1071. doi:10.1357/0022240963213763

Goni, G.J., Garzoli, S.L., Roubicek, A.J., Olson, D.B., Brown, O.B., 1997. Agulhas ring dynamics from TOPEX/POSEIDON satellite altimeter data. Journal of Marine Research 55, 861–883. doi:10.1357/0022240973224175

Gordon, A.L., 1989. Brazil-Malvinas Confluence-1984. Deep Sea Research 36, 359–384. https://doi.org/10.1016/0198-0149(89)90042-3

Gordon, A.L., 1986. Interocean exchange of thermocline water. Journal of Geophysical Research 91, 5037–5046. https://doi.org/10.1029/JC091iC04p05037

Gordon, A.L., 1985a. Indian-Atlantic Transfer of Thermocline Water at the Agulhas Retroflection. Science 227, 1030–1033. doi:10.1126/science.227.4690.1030

Gordon, A.L., 1985b. Indian-Atlantic Transfer of Thermocline Water at the Agulhas Retroflection. Science 227, 1030–1033. doi:10.1126/science.227.4690.1030

Gordon, A.L., 1981. South Atlantic thermocline ventilation. Deep Sea Research I 28A, 1239–1264. https://doi.org/10.1016/0198-0149(81)90033-9

Gordon, A.L., Bosley, K.T., Aikman, F., III, 1995. Tropical Atlantic water within the Benguela upwelling system at 27S. Deep-Sea Research I 42, 1–12. doi:10.1016/0967-0637(94)00032-N

Gordon, A.L., Haxby, W.F., 1990. Agulhas eddies invade the south Atlantic: Evidence From Geosat altimeter and shipboard conductivity-temperature-depth survey. Journal of Geophysical Research 95, 3117–3125.

Gordon, A.L., Weiss, R.F., Smethie, W.M., Jr, Warner, M.J., 1992. Thermocline and intermediate water communication between the South Atlantic and Indian Oceans. Journal of Geophysical Research 97, 7223–7240. doi:10.1029/92JC00485

Hernández-Guerra, A., Espino-Falcón, E., Vélez-Belchí, P., Pérez-Hernández, M.D., Martínez-Marrero, A., Cana, L., 2017. Recirculation of the Canary Current in fall 2014. Journal of Marine Systems 174, 25–39. doi:10.1016/j.jmarsys.2017.04.002

Hernández-Guerra, A., Fraile-Nuez, E., López-Laatzen, F., Martínez, A., Parrilla, G., Vélez-Belchí, P., 2005. Canary Current and North Equatorial Current from an inverse box model. Journal of Geophysical Research 110. doi:10.1029/2005JC003032

Hernández-Guerra, A., Joyce, T.M., Fraile-Nuez, E., Vélez-Belchí, P., 2010. Using Argo data to investigate the Meridional Overturning Circulation in the North Atlantic. Deep-Sea Res Pt I 57, 29–36. doi:10.1016/j.dsr.2009.10.003

Hernández-Guerra, A., Nykjaer, L., 1997. Sea surface temperature variability off north-west Africa: 1981-1989. International Journal of Remote Sensing 18, 2539–2558.

Hernández-Guerra, A., Pelegrí, J.L., Fraile-Nuez, E., Benítez-Barrios, V.M., Emelianov, M., Pérez-Hernández, M.D., Vélez-Belchí, P., 2014. Meridional Overturning Transports at 7.5N and 24.5N in the Atlantic Ocean during 1992-93 and 2010-11. Prog Oceanogr 128, 98–114. doi:10.1016/j.pocean.2014.08.016

Hernández-Guerra, A., Talley, L., 2016. Meridional overturning transports at 30°S in the Indian and Pacific Oceans in 2002-2003 and 2009. Prog Oceanogr 146, 89–120. doi:10.1016/j.pocean.2016.06.005

Heywood, K.J., King, B.A., 2002. Water masses and baroclinic transports in the South Atlantic and Southern oceans. Journal of Marine Research 60, 639–676.

Hogg, N., Biscaye, P., Gardner, W., Schmitz, W.J., Jr, 1982. On the transport and modification of Antarctic Bottom Water in the Vema Channel. Journal of Marine Research 40, 231–263.

Hogg, N., Owens, W., 1999. Direct measurement of the deep circulation within the Brazil Basin. Deep Sea Research Part II: Topical Studies in Oceanography 46, 335–353.

Hogg, N., Siedler, G., Zenk, W., 1999. Circulation and variability at the southern boundary of the Brazil Basin. J. Phys. Oceanogr. 29, 145–157.

Hogg, N.G., Thurnherr, A.M., 2005. A Zonal Pathway for NADW in the South Atlantic. J Oceanogr 61, 493–507. doi:10.1007/s10872-005-0058-7

Holfort, J., Siedler, G., 2001. The meridional oceanic transports of heat and nutrients in the South Atlantic. J. Phys. Oceanogr. 31, 5–29.

Jackett, D.R., McDougall, T.J., 1997. A Neutral Density Variable for the World's Oceans. J. Phys. Oceanogr. 27, 237–263.

Johnson, G.C., 2008. Quantifying Antarctic Bottom Water and North Atlantic Deep Water volumes. Journal of Geophysical Research 113. doi:10.1029/2007JC004477

Joyce, T., Hernández-Guerra, A., Smethie, W., 2001. Zonal circulation in the NW Atlantic and Caribbean from a meridional World Ocean Circulation Experiment hydrographic section at 66 degrees W. J Geophys Res-Oceans 106, 22095–22113.

Kalnay, E., Kanamitsu, M., Kistler, R., collins, W., Deaven, D., Gandin, L., Iredell, M., Saha, S., White, G., Woollen, J., Zhu, Y., Chellah, M., Ebisuzaki, W., Higgins, W., Janowiak, J., Mo, K.C., Ropelewski, C., Wang, J., Leetmaa, A., Reynolds, R., Jenne, R., Joseph, D., 1996. The NCEP/NCAR 40-year reanalysis project 77, 437–471.

Kanzow, T., Cunningham, S.A., Rayner, D., Hirschi, J.J.M., Johns, W.E., Baringer, M.O., Bryden, H.L., Beal, L.M., Meinen, C.S., Marotzke, J., 2007. Observed flow compensation associated with the MOC at 26.5°N in the Atlantic. Science 317, 938–941. doi:10.1126/science.1141304

Katsumata, K., Fukasawa, M., 2011. Changes in meridional fluxes and water properties in the Southern Hemisphere subtropical oceans between 1992/1995 and 2003/2004. Prog Oceanogr 89, 61–91. doi:10.1016/j.pocean.2010.12.008

Katsumata, K., Sloyan, B., Masuda, S., 2013. Diapycnal and isopycnal transports in the Southern Ocean estimated by a box inverse model. Journal of Physical Oceanography 43, 2270–2287. doi:10.1175/JPO-D-12-0210.1

Koltermann, K.P., Gouretski, V., Jancke, K., 2011. Hydrographic Atlas of the World Ocean Circulation Experiment (WOCE). Volume 3: Atlantic Ocean. Southampton, UK. https://doi.org/10.21976/C6RP4Z

Larqué, L., Maamaatuaiahutapu, K., Garcon, V., 1997. On the intermediate and deep water flows in the South Atlantic Ocean. Journal of Geophysical Research 102, 12425–12440.

las Heras, de, M.W., Schlitzer, R., 1999. On the importance of intermediate water flows for the global ocean overturning. Journal of Geophysical Research 104, 15515–15536.

Laxenaire, R., Speich, S., Blanke, B., Chaigneau, A., Pegliasco, C., Stegner, A., 2018. Anticyclonic Eddies Connecting the Western Boundaries of Indian and Atlantic Oceans. J Geophys Res-Oceans 123, 7651–7677. doi:10.1029/2018JC014270

Lumpkin, R., Speer, K., 2007. Global ocean meridional overturning. J. Phys. Oceanogr. 37, 2550–2562. doi:10.1175/JPO3130.1

Macdonald, A., 1998. The global ocean circulation: a hydrographic estimate and regional analysis. Prog Oceanogr 41, 281–382.

Macdonald, A., 1993. Property Fluxes at 30-Degrees-S and Their Implications for the Pacific-Indian Throughflow and the Global Heat-Budget. J Geophys Res-Oceans 98, 6851–6868.

Macdonald, A., Wunsch, C., 1996. An estimate of global ocean circulation and heat fluxes. Nature 382, 436–439.

Macdonald, A.M., Mecking, S., Robbins, P.E., Toole, J.M., Johnson, G.C., Talley, L., Cook, M., Wijffels, S.E., 2009. The WOCE-era 3-D Pacific Ocean circulation and heat budget. Prog Oceanogr 82, 281–325. doi:10.1016/j.pocean.2009.08.002

Machín, F., Pelegrí, J.L., Fraile-Nuez, E., Vélez-Belchí, P., López-Laatzen, F., Hernández-Guerra, A., 2010. Seasonal flow reversals of Intermediate Waters in the Canary Current System east of the Canary Islands. J. Phys. Oceanogr. 40, 1902–1909.

Mantyla, A.W., Reid, J.L., 1983. Abyssal characteristics of the World Ocean waters. Deep-Sea Res 30, 805–833.

Mazloff, M.R., Heimbach, P., Wunsch, C., 2010. An Eddy-Permitting Southern Ocean State Estimate. J. Phys. Oceanogr. 40, 880–899. doi:10.1175/2009JPO4236.1

McCartney, M.S., 1993. Crossing of the equator by the deep western boundary current in the western Atlantic Ocean. J. Phys. Oceanogr. 23, 1953–1974.

McDonagh, E.L., Arhan, M., Heywood, K.J., 2002. On the circulation of bottom water in the region of the Vema Channel. Deep-Sea Research I 49, 1119–1139. doi:10.1016/S0967-0637(02)00016-X

McDonagh, E.L., King, B.A., 2005. Oceanic fluxes in the South Atlantic. J. Phys. Oceanogr. 35, 109–122. doi:10.1175/JPO-2666.1

Meinen, C.S., Garzoli, S.L., 2014. Attribution of Deep Western Boundary Current variability at 26.5°N. Deep-Sea Research I 90, 81–90. doi:10.1016/j.dsr.2014.04.016

Meinen, C.S., Garzoli, S.L., Perez, R.C., Campos, E., Piola, A.R., Chidichimo, M.P., Dong, S., Sato, O.T., 2017. Characteristics and causes of Deep Western Boundary Current transport variability at 34.5°S during 2009–2014. Ocean Sci. 13, 175–194. doi:10.5194/os-13-175-2017

Meinen, C.S., Speich, S., Perez, R.C., Dong, S., Piola, A.R., Garzoli, S.L., Baringer, M.O., Gladyshev, S., Campos, E.J.D., 2013. Temporal variability of the meridional overturning circulation at 34.5°S: Results from two pilot boundary arrays in the South Atlantic. J Geophys Res-Oceans 118, 6461–6478. doi:10.1002/2013JC009228

Meinen, C.S., Speich, S., Piola, A.R., Ansorge, I., Campos, E., Kersalé, M., Terre, T., Chidichimo, M.P., Lamont, T., Sato, O.T., Perez, R.C., Valla, D., van den Berg, M., Le Hénaff, M., Dong, S., Garzoli, S.L., 2018. Meridional Overturning Circulation Transport Variability at 34.5°S During 2009-2017: Baroclinic and Barotropic Flows and the Dueling Influence of the Boundaries. Geophysical Research Letters 45. doi:10.1029/2018GL077408

Munk, W.H., 1950. On the wind-driven ocean circulation. Journal of Meteorology 7, 79–93.

Müller, T.J., ikeda, Y., Zangenberg, N., Nonato, L.V., 1998. Direct measurements of western boundary currents off Brazil between 20°S and 28°S. Journal of Geophysical Research 103, 5429–5437.

Nelson, G., Hutchings, L., 1983. The Benguela upwelling area. Progress in Oceanography 12, 333–356. https://doi.org/10.1016/0079-6611(83)90013-7

Peterson, R.G., 1992. The boundary currents in the western Argentine Basin. Deep Sea Research 39, 623–644. doi:10.1016/0198-0149(92)90092-8

Peterson, R.G., Stramma, L., 1991. Upper-level circulation in the South Atlantic Ocean. Prog Oceanogr 26, 1–73. doi:10.1016/0079-6611(91)90006-8

Peterson, R.G., Whitworth, T., III, 1989. The subantarctic and polar fronts in relation to deep water masses through the southwestern Atlantic. Journal of Geophysical Research 94, 10817–10838. doi:10.1029/JC094iC08p10817

Pickart, R.S., 1992. Water mass components of the North Atlantic deep western boundary current. Deep-Sea Res 39, 1553–1572.

Poole, R., Tomczak, M., 1999. Optimum multiparameter analysis of the water mass structure in the Atlantic Ocean thermocline. Deep-Sea Research I 46, 1895–1921.

Reid, J., 2003. On the total geostrophic circulation of the Indian Ocean: flow patterns, tracers, and transports. Prog Oceanogr 56, 137–186. doi:10.1016/S0079-6611(02)00141-6

Reid, J., 1994. On the Total Geostrophic Circulation of the North-Atlantic Ocean - Flow Patterns, Tracers, and Transports. Prog Oceanogr 33, 1–92.

Reid, J., Nowlin, W.D., Jr, Patzert, W.C., 1977. On the characteristics and circulation of the southwestern Atlantic Ocean. J. Phys. Oceanogr. 7, 62–91.

Reid, J.L., 1997. On the total geostrophic circulation of the pacific ocean: flow patterns, tracers, and transports. Prog Oceanogr 39, 263–352. doi:10.1016/S0079-6611(97)00012-8

Reid, J.L., 1989. On the total geostrophic circulation of the South Atlantic Ocean: Flow patterns, tracers, and transports. Prog Oceanogr 23, 149–244.

Richardson, P.L., 2007. Agulhas leakage into the Atlantic estimated with subsurface floats and surface drifters. Deep-Sea Res Pt I 54, 1361–1389. doi:10.1016/j.dsr.2007.04.010

Rintoul, S., 1991. South Atlantic Interbasin Exchange. Journal of Geophysical Research 96, 2675–2692.

Roemmich, D., Wunsch, C., 1985. Two transatlantic sections: Meridional circulation and heat flux in the subtropical North Atlantic Ocean. Deep-Sea Research 32, 619–664. doi: 10.1016/0198-0149(85)90070-6

Saunders, P.M., King, B.A., 1995. Oceanic fluxes on the WOCE A11 section. J. Phys. Oceanogr. 25, 1942–1958.

Schmitz, W., 1995. On the Interbasin-Scale Thermohaline Circulation. Rev Geophys 33, 151–173.

Schmitz, W., McCartney, M.S., 1993. On the North Atlantic Circulation. Rev Geophys 31, 29–49.

Shannon, L.V., Hunter, D., 1988. Notes on Antarctic intermediate water around southern Africa. South African Journal of Marine Science 6, 107–117. doi:10.2989/025776188784480735

Smethie, W.M., Fine, R.A., Putzka, A., Jones, E.P., 2000. Tracing the flow of North Atlantic Deep Water using chlorofluorocarbons. J Geophys Res-Oceans 105, 14297–14323.

Speer, K., Zenk, W., Siedler, G., Pätzold, J., Heidland, C., 1992. First resolution of flow through the Hunter Channel in the South Atlantic. Earth and Planetary Science Letters 113, 287–292. doi:10.1016/0012-821X(92)90226-L

Speer, K.G., Siedler, G., Talley, L., 1995. The Namib Col Current. Deep-Sea Research I 42, 1933–1950.

Speer, K.G., Zenk, W., 1993. The flow of Antarctic bottom water into the Brazil Basin. J. Phys. Oceanogr. 23, 2667–2682.

Sprintall, J., Tomczak, M., 1993. On the formation of Central Water and thermocline ventilation in the southern hemisphere. Deep Sea Research I 40, 827–848. https://doi.org/10.1016/0967-0637(93)90074-D

Stommel, H., 1948. The westward intensification of wind-driven ocean currents. Transactions, American Geophysical Union 29, 202–206.

Stommel, H., Arons, A.B., Faller, A.J., 1958. Some Examples of Stationary Planetary Flow Patterns in Bounded Basins. Tellus 10, 179–187.

Stramma, L., 1989. The Brazil Current transport south of 23S. Deep Sea Research 36, 639–646.

Stramma, L., England, M., 1999. On the water masses and mean circulation of the South Atlantic Ocean. Journal of Geophysical Research 104.

Stramma, L., Peterson, R.G., 1990. The South Atlantic Current. J. Phys. Oceanogr. 20, 846–859.

Stramma, L., Peterson, R.G., 1989. Geostrophic transport in the Benguela Current region. J. Phys. Oceanogr. 19, 1440–1448.

Suga, T., Talley, L., 1995. Antarctic Intermediate Water circulation in the tropical and subtropical South Atlantic. Journal of Geophysical Research 100, 13441–13453. doi:10.1029/95JC00858

Sverdrup, H.U., 1947. Wind-Driven Currents in a Baroclinic Ocean; with Application to the Equatorial Currents of the Eastern Pacific. Proceedings of the National Academy of Sciences of the United States of America 33, 318–326.

Talley, L., 2013. Closure of the Global Overturning Circulation Through the Indian, Pacific, and Southern Oceans: Schematics and Transports. Oceanog 26, 80–97. doi:10.5670/oceanog.2013.07

Talley, L., 2008. Freshwater transport estimates and the global overturning circulation: Shallow, deep and throughflow components. Prog Oceanogr 78, 257–303. doi:10.1016/j.pocean.2008.05.001

Talley, L., 2003. Shallow, intermediate, and deep overturning components of the global heat budget. J. Phys. Oceanogr. 33, 530–560.

Talley, L., 1996. Antarctic Intermediate Water in the South Atlantic, in: Wefer, G., Berger, W.H., Siedler, G., Webb, D. (Eds.), The South Atlantic. Present and Past Circulation. Springer, Berlin, Heidelberg, Berlin, Heidelberg, pp. 219–238. doi:10.1007/978-3-642-80353-6_11

Talley, L., Feely, R.A., Sloyan, B.M., Wanninkhof, R., Baringer, M.O., Bullister, J.L., Carlson, C.A., Doney, S.C., Fine, R.A., Firing, E., Gruber, N., Hansell, D.A., Ishii, M., Johnson, G.C., Katsumata, K., Key, R.M., Kramp, M., Langdon, C., Macdonald, A.M., Mathis, J.T., McDonagh, E.L., Mecking, S., Millero, F.J., Mordy, C.W., Nakano, T., Sabine, C.L., Smethie, W.M., Swift, J.H., Tanhua, T., Thurnherr, A.M., Warner, M.J., Zhang, J.Z., 2016. Changes in Ocean Heat, Carbon Content, and Ventilation: A Review of the First Decade of GO-SHIP Global Repeat Hydrography. Annu. Rev. Marine. Sci. 8. doi:10.1146/annurev-marine-052915-100829

Talley, L., McCartney, M.S., 1982. Distribution and circulation of Labrador Sea water. J. Phys. Oceanogr. 12, 1189–1205.

Talley, L., Pickard, G., Emery, W., Swift, J., 2011. Descriptive physical oceanography: An introduction, Sixth. ed. Elsevier Ltd, Boston.

Talley, L., Reid, J.L., Robbins, P.E., 2003. Data-based meridional overturning streamfunctions for the global ocean. Journal of Climate 16, 3213–3226.

Tamsitt, V., Drake, H.F., Morrison, A.K., Talley, L., Dufour, C.O., Gray, A.R., Griffies, S.M., Mazloff, M.R., Sarmiento, J.L., Wang, J., Weijer, W., 2017. Spiraling pathways of global deep waters to the surface of the Southern Ocean. Nature Communications 8, 1–10. doi:10.1038/s41467-017-00197-0

Tsuchiya, M., Talley, L., McCartney, M.S., 1994. Water-mass distributions in the western South Atlantic; A section from South Georgia Island (54S) northward across the equator. Journal of Marine Research 52, 55–81. https://doi.org/10.1357/0022240943076759

van Sebille, E., Johns, W.E., Beal, L.M., 2012. Does the vorticity flux from Agulhas rings control the zonal pathway of NADW across the South Atlantic? Journal of Geophysical Research 117. doi:10.1029/2011JC007684

Vanicek, M., Siedler, G., 2002. Zonal Fluxes in the Deep Water Layers of the Western South Atlantic Ocean. J. Phys. Oceanogr. 32, 2205–2235.

Warner, M.J., Weiss, R.F., 1992. Chlorofluoromethanes in South Atlantic Antartic intermediate water. Deep-Sea Research 39, 2053–2075. https://doi.org/10.1016/0198-0149(92)90013-J

Warren, B.A., Speer, K.G., 1991. Deep circulation in the eastern South Atlantic Ocean. Deep-Sea Res 38, S281–S322. doi:10.1016/S0198-0149(12)80014-8

Weeks, S.J., Barlow, R., Roy, C., Shillington, F.A., 2006. Remotely sensed variability of temperature and chlorophyll in the southern Benguela: upwelling frequency and phytoplankton response. African Journal of Marine Science 28, 493–509. doi:10.2989/18142320609504201

Wunsch, C., 1996. The ocean circulation inverse problem. Cambridge University Press.

Wunsch, C., 1978. North-Atlantic General Circulation west of 50W determined by inverse methods. Rev Geophys 16, 583–620.

Wunsch, C., 1977. Determining the general circulation of the oceans: A preliminary discussion. Science 196, 871–875.

Zangenberg, N., Siedler, G., 1998. Path of the North Atlantic Deep Water in the Brazil Basin. Journal of Geophysical Research: Oceans (1978–2012) 103, 5419–5428. doi:10.1029/97JC03287

Zemba, J.C., 1991. The Structure and Transport of the Brazil Current Between 27 and 36 South.

Zenk, W., Siedler, G., Lenz, B., Hogg, N., 1999. Antarctic Bottom Water Flow through the Hunter Channel. Journal of Physical Oceanography 29, 2785–2801.

Table 1. Hydrographic cruise information. Data were collected through the Carbon Hydrographic Data Office (CCHDO) (http://cchdo.ucsd.edu). LADCP data are available online through the CLIVAR LADCP archive (http://currents.soest.hawaii.edu/clivar/ladcp/).

	Dates	No. Stations	CCHDO Expocode	Ship	Chief Scientists
A10-2003	2003-11-06 to 2003-12-05	111	49NZ20031106	Mirai	Y. Yoshikawa (JAMSTEC, Japan)
A10-2011	2011-09-26 to 2011-10-31	120	33RO20110926	Ronald H. Brown	M. Baringer (AOML, USA) A. Macdonald (WHOI, USA)

Table 2. Ekman transport (Sv) averaged during the time of the cruise at 30°S in the Atlantic Ocean using NCEP wind stress and adjusted Ekman transport after the inverse model C.

Ekman transport (Sv)	A10-2003	A10-2011
Time of the cruise	-0,2±0,04	-0,3±0,06
Model C	-0,3±0,04	-0,3±0,04

Table 3. Constraints for inverse models A and B. Constraints for model A come from (Talley, 2008) (her Table 14). Constraints for model B come from Mazloff et al. (2010).

Layer	Neutral density (γ^n) range	Talley (2008) Model A	Mazloff et al. (2010) Model B
		Constraint	Constraint
0	Ekman trans.	1.15±0.23	(In layer 1)
1	Surf-26.14	1.77±0.54	3.27±3.55
2	26.14-26.45	0.12±0.56	1.14±0.38
3	26.45-27.0	4.55±1.07	3.51±0.89
4	27.0-27.23	2.47±0.67	2.12±0.39
5	27.23-27.58	2.71±1.82	3.27±0.55
6	27.58-27.84	-2.45±1.74	0.54±0.64
7	27.84-28.04	-10.16±4.81	-6.19±2.82
8	28.04-28.10	-5.03±2.10	-6.00±1.36
9	28.10-28.15	0.86±0.87	-3.95±2.79
10	28.15-28.23	2.33±0.93	1.08±3.01
11	28-23-bot.	0.67±0.15	0±0
Total	Surf-bot.	-1.00±0.6	-1.21±0.6

Table 4. Regional transport constraints applied to every model. Initial geostrophic transport (with the reference layer at γ^n=28.1 kg/m^3) and final geostrophic transport after every inverse model. Positive transports are northward. The western and eastern boundary currents are LADCP-based transport constraints and are cruise-dependent.

Constraint (Sv)	Longitude	Layers	Constraint	2003 Initial	2003 Final	2011 Initial	2011 Final	Model
Bering Transport	All	1:11	-1.0±0.6	36.4	-1.0±2.6	38.6	-1.1±2.7	A
			-1.2±0.6		-1.2±2.8		-1.2±2.9	B
			-0.8±0.6		-0.8±4.5		-0.8±5.0	C
Vema Channel[a]	~39.7-37.7W	9:11	4.0±0.4	1.8	3.7±0.3	3.8	3.5±0.3	A
					3.6±0.3		3.2±0.3	B
					3.8±0.4		4.0±0.4	C
Brazil Basin[b]	~45-15.3W	9:11	6.9±1.8	5.1	5.7±1.4	8.3	6.9±1.5	A
					5.5±1.8		6.0±2.0	B
					6.4±2.0		6.6±2.4	C
Walvis R. North[c]	~7.3W-1.7E	9:11	0±1	-0.8	-0.2±0.8	-0.8	-1.3±0.8	A
					-1.3±0.9		-2.1±0.9	B
					-0.3±0.9		-0.2±0.9	C
Walvis R. South[c]	~2.2-13.4E	9:11	0±1	3.5	-0.5±1.0	3.3	-0.6±1.1	A
					-0.5±1.1		-1.0±1.2	B
					-0.1±1.2		0.0±1.2	C
Brazil Current[d] 2003 2011	Coast to 44.8W Coast to 46.3W	1:7 1:5	-40.8±5 -12.7±5	-28.7	-37.3±2.0	-9.9	-10.4±0.7	A
					-33.6±2.0		-13.4±0.8	B
					-38.9±2.1		-10.4±0.8	C
Benguela Current[d] 2003 2011	Coast to 11.8E Coast to 11.3E	1:7 1:7	27.4±5 22.7±5	27.2	27.5±2.3	28.2	28.2±2.4	A
					30.1±2.3		33.1±2.4	B
					26.3±2.4		22.5±2.5	C

[a] Bottom transport constraint in the Vema Channel from Hogg et al. (1982).

[b] Bottom transport constraint in the Brazil Basin from Hogg and Owens (1999)

[c] Bathymetric constraint (Warren and Speer, 1991)

[d] Boundary currents constraints from cruise-based LADCP profiles.

Table 5. Mass transport and uncertainty (Sv) in 2003 and 2011 for all neutral density layers for the three inverse models (A, B, C).

Layer	Neutral density (γ^n) range	Model	Mass Transport (Sv)	Mass Transport (Sv)
			2003	2011
1+Ekman Tr.	Surface-26.14	A	0.95±0.34	0.48±0.40
		B	-0.56±0.40	-2.12±0.52
		C	-0.77±0.51	-2.63±0.60
2	26.14-26.45	A	4.29±0.28	4.95±0.36
		B	3.55±0.24	4.07±0.29
		C	5.69±0.36	8.71±0.49
3	26.45-27.0	A	4.82±0.46	5.94±0.44
		B	4.57±0.42	5.87±0.39
		C	5.39±0.66	7.08±0.72
4	27.0-27.23	A	1.88±0.26	2.07±0.27
		B	2.19±0.20	2.44±0.21
		C	1.95±0.41	2.15±0.41
5	27.23-27.58	A	1.38±0.59	0.01±0.54
		B	2.78±0.39	1.71±0.35
		C	1.16±0.86	1.02±0.88
6	27.58-27.84	A	-2.91±0.57	-3.38±0.58
		B	-0.98±0.42	-0.77±0.41
		C	-3.15±0.83	-3.12±0.90
7	27.84-28.04	A	-10.92±1.44	-11.43±1.51
		B	-9.37±1.36	-8.99±1.40
		C	-10.70±1.84	-13.25±1.90
8	28.04-28.10	A	-4.62±1.54	-4.60±1.61
		B	-5.88±1.14	-6.19±1.16
		C	-5.61±2.87	-7.00±3.20
9	28.10-28.15	A	0.32±0.74	0.99±0.76
		B	-2.44±1.24	-0.84±1.41
		C	-1.28±1.55	-2.07±1.84
10	28.15-28.23	A	3.08±0.82	2.69±0.83
		B	4.98±1.48	3.57±1.61
		C	5.42±1.88	5.06±2.12
11	28-23-bottom	A	0.70±0.13	1.13±0.13
		B	0±0	0±0
		C	1.12±0.28	3.27±0.32
Total	Surf.-bottom	A	-1.04±2.62	-1.15±2.71
		B	-1.16±2.76	-1.24±2.95
		C	-0.78±4.48	-0.79±4.97

Table 6. Net mass transport and uncertainty (Sv) for thermocline and intermediate layers flowing to the north, deep layers flowing to the south and bottom layer flowing to the north for every model and year.

Mass Transport (Sv)

	2003			2011		
	Model A	Model B	Model C	Model A	Model B	Model C
Thermoc.+Interm. ($\gamma^n<27.58$ kg/m^3)	13.3±0.9	12.5±0.8	13.4±1.3	13.4±0.9	12.0±0.8	16.3±1.4
Deep ($27.58<\gamma^n<28.15$ kg/m^3)	-18.5±2.2	-18.7±2.2	-20.7±3.8	-19.4±2.3	-16.8±2.3	-25.4±4.2
Bottom ($\gamma^n>28.15$ kg/m^3)	4.1±1.1	5.0±1.5	6.5±1.9	4.8±1.1	3.6±1.6	8.3±2.1

Table 7. Initial, LADCP-adjusted and results of every inverse model mass transport (Sv) for the Brazil Current in the surface and thermocline layers, Antarctic Intermediate Water (AAIW) and Upper Circumpolar Deep Water (UCDW) layers for 2003 and 2011.

		Brazil Current (Sv)				
		Initial	LADCP-adjusted	Model A	Model B	Model C
Sf+Thermocline	2003	-17.2	-20.4	-20.1±0.7	-19.9±0.7	-20.2±0.7
(layers 1:4)	2011	-9.4	-12.0	-9.9±0.6	-12.7±0.6	-9.7±0.7
AAIW	2003	-3.9	-5.7	-5.3±0.7	-4.7±0.7	-5.5±0.7
(layer 5)	2011	-0.5	-0.7	-0.5±0.4	-0.7±0.4	-0.6±0.4
UCDW	2003	-4.2	-7.3	-5.9±0.9	-4.7±0.9	-6.3±0.9
(layer 6)	2011	-0.0	-0.1	0.1±0.4	0.1±0-4	0.1±0.4

Table 8. Mass transport (Sv) for the Benguela Current in the surface and thermocline layers, and the Antarctic Intermediate Water layer in 2003 and 2011 as result of the inverse models.

		Benguela Current (Sv) (~3°-15°E)		
		Model A	Model B	Model C
Sf+Thermocline (Layers 1:4)	2003	15.6±0.9	15.4±0.9	15.6±0.9
	2011	11.7±0.8	12.1±0.8	11.2±0.8
AAIW (layer 5)	2003	2.5±0.9	3.4±0.9	1.9±0.9
	2011	1.9±0.8	3.3±0.8	1.0±0.8

Table 9. Mass transport (Sv) for the Deep Western Boundary Current (DWBC) and its recirculation for every inverse model and year. The longitude shown is the eastern boundary of the currents in 2003 and 2011.

		Model A	Model B	Model C
DWBC	2003 (~39.8°W)	-27.5±4.0	-35.3±3.4	-16.1±5.1
	2011 (~39.1°W)	-30.2±3.8	-44.4±3.7	---
Recirculation	2003 (~38.9°W)	9.8±1.4	10.9±1.3	8.4±1.1
	2011 (~37.8°W)	14.9±1.6	23.5±1.6	---

Table 10. Mass transport (Sv) for the North Atlantic Deep Water (NADW) west of the Mid-Atlantic Ridge (MAR) and east of the MAR in 2003 and 2011 and as solution of the inverse models.

		NADW transport (Sv)		
		Model A	Model B	Model C
West of MAR	2003	-8.5±4.6	-3.0±4.7	-12.5±5.5
	2011	-7.1±4.8	-5.7±4.9	-12.8±5.5
East of MAR	2003	-10.0±4.6	-15.6±4.6	-8.2±5.6
	2011	-12.3±4.7	-11.1±4.8	-12.7±5.5

Figures

Figure 1. Station positions for A10 cruises carried out at 30°S in 2003 and 2011.

Figure 2. Vertical sections of potential temperature (°C) at 30°S in the Atlantic Ocean for (a) 2003 and (b) 2011.

Figure 3. Vertical sections of salinity at 30°S in the Atlantic Ocean for (a) 2003 and (b) 2011.

Figure 4. Vertical sections of neutral density (γ^n) at 30°S in the Atlantic Ocean for (a) 2003 and (b) 2011.

Figure 5. Vertical sections of oxygen (µM/kg) at 30°S in the Atlantic Ocean for (a) 2003 and (b) 2011.

Figure 6. Vertical sections of silicate (µM/kg) at 30°S in the Atlantic Ocean for (a) 2003 and (b) 2011.

Figure 7. Initial zonally-integrated meridional mass transport (Sv) per layer across 30°S during 2003 and 2011.

Figure 8. Zonally-integrated meridional mass transport (Sv) per layer across 30°S used as constraint for model A from Talley (2008) and model B from Mazloff et al. (2010).

Figure 9. Comparison between the initial geostrophic velocity profile (black lines), the LADCP velocity normal to the station pairs (blue line) and the geostrophic velocity adjusted to the LADCP data (red line, with the depth range used for LADCP referencing between the horizontal dashed lines). The subplots (a, b) and (c, d) correspond to selected station pairs of the Brazil and Benguela Currents, respectively.

Figure 10. Reference velocities (m s^{-1}) with error bars as a function of longitude for all models, for the 2003 and 2011 sections at 30°S in the Atlantic Ocean.

Figure 11. Final zonally-integrated meridional mass transport (Sv) per layer, with error bars, across 30°S during 2003 and 2011, for all three inverse models.

Figure 12. Overturning mass transports across 30°S for the Atlantic Ocean for all models and years, computed as the zonally- and vertically-integrated mass transports in isoneutral layers (along the entire section and from the sea surface to the seafloor).

Figure 13. Vertical sections of velocity (cm/s) along 30°S in 2003 (left subplots) and 2011 (right subplots) as deduced by all three inverse models. Notice the change in vertical scale, with an expanded view of the top 1250 m of the water column. Contours are drawn every 10 cm/s with solid/dashed contours representing positive/negative values that correspond to northward/southward velocities. The colorbar is on the left of subplot (c).

Figure 14. a) Mean Absolute Dynamic Topography (ADT) for November 2003; b) ADT for 8/11/2003, at the time of the hydrographic stations carried out in the western boundary in 2003; c) ADT for 01/12/2003, at the time of the hydrographic stations carried out in the eastern boundary in 2003; d) mean ADT for September/October 2011; e) ADT for 20/10/2011, at the time of the hydrographic stations carried out in the western boundary in 2011; and f) ADT for 29/09/2011, at the time of the hydrographic stations carried out in the eastern stations in 2011.

Figure 15. Accumulated mass transports (from the west) for the shallowest layer as estimated from the inverse models and as inferred from the Absolute Dynamic Topography (ADT) from Figure 14. The velocity data for the ocean interior come from the mean ADT and the velocity data for the western and eastern boundaries come from the ADT at the time when the hydrographic stations were carried out.

Figure 16. Eastward accumulated mass transport (Sv) at 30°S for (a) upper, (b) deep, and (c) bottom layers for 2003 (solid lines) and 2011 (dashed lines) for all models. The

deep and bottom layers for model A are not the same as in models B and C (see text for explanation). Bottom plot shows the bathymetry for reference.

Figure 17. Mass transport (Sv) per layer corresponding to the Brazil Current. (a) Relative (dashed line) and adjusted to LADCP velocity profile (solid line) for 2003 (blue line) and 2011 (red line). (b) Model velocities for 2003 (solid lines) and 2011 (dashed lines).

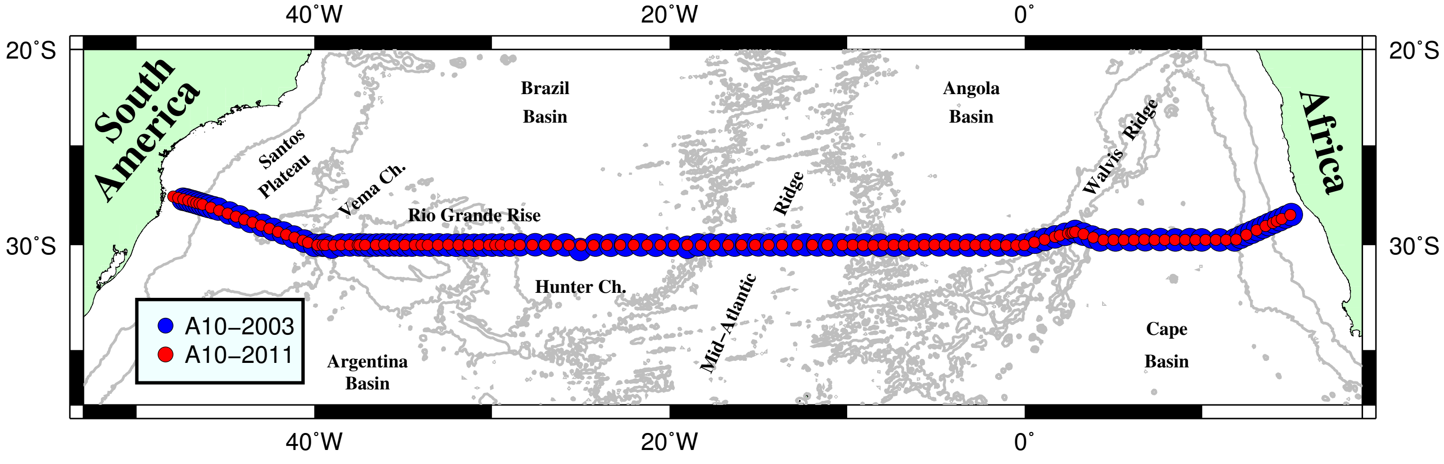

Atlantic Ocean (A10–30^{o}S)

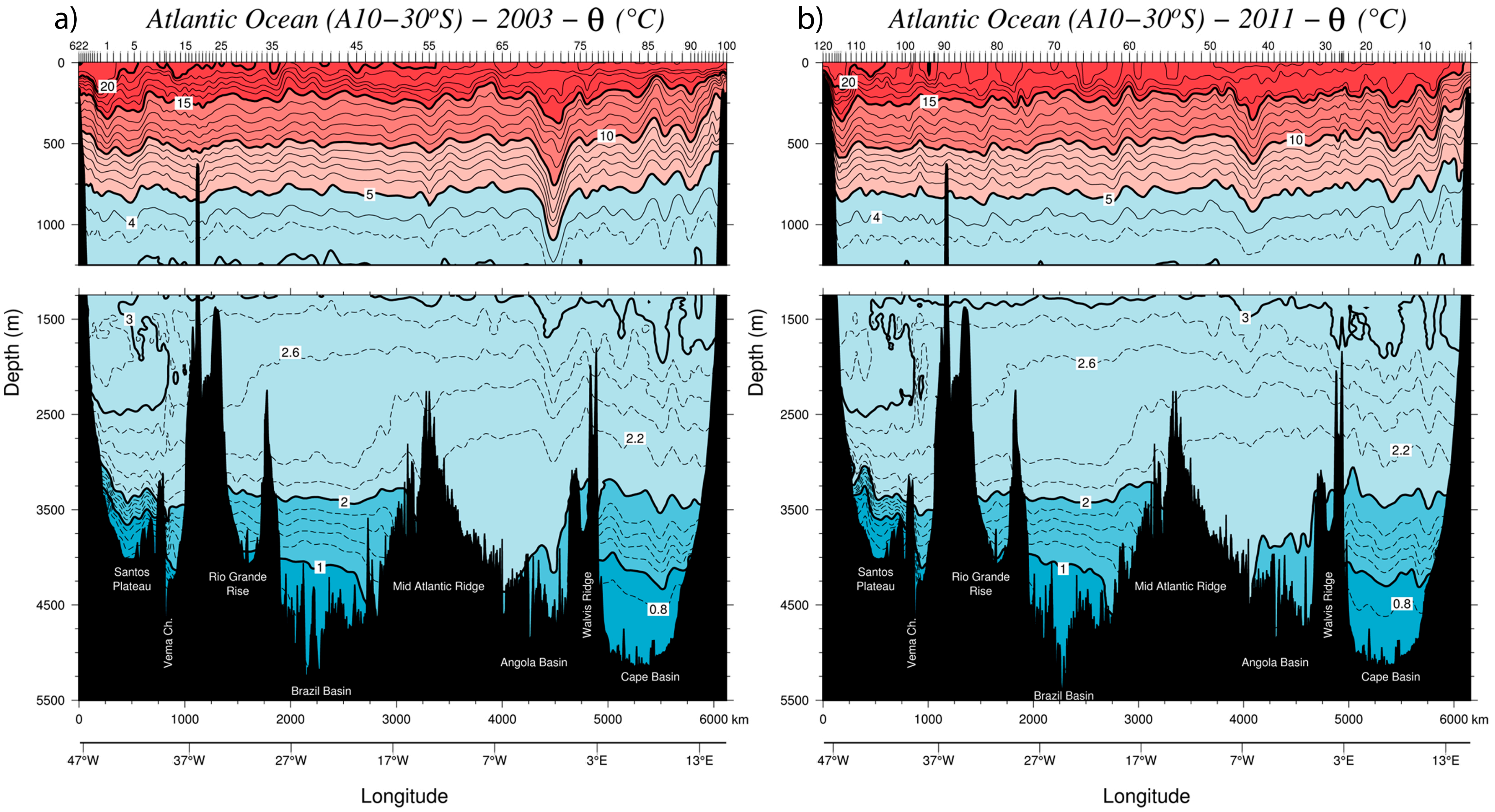
a)
Atlantic Ocean (A10–30°S) – 2003 – θ (°C)
b)
Atlantic Ocean (A10–30°S) – 2011 – θ (°C)
Depth (m)
0
500
1000
1500
2500
3500
4500
5500
20
15
10
5
4
3
2.6
2.2
2
1
0.8
Santos Plateau
Vema Ch.
Rio Grande Rise
Brazil Basin
Mid Atlantic Ridge
Angola Basin
Walvis Ridge
Cape Basin
0
1000
2000
3000
4000
5000
6000 km
47°W
37°W
27°W
17°W
7°W
3°E
13°E
Longitude

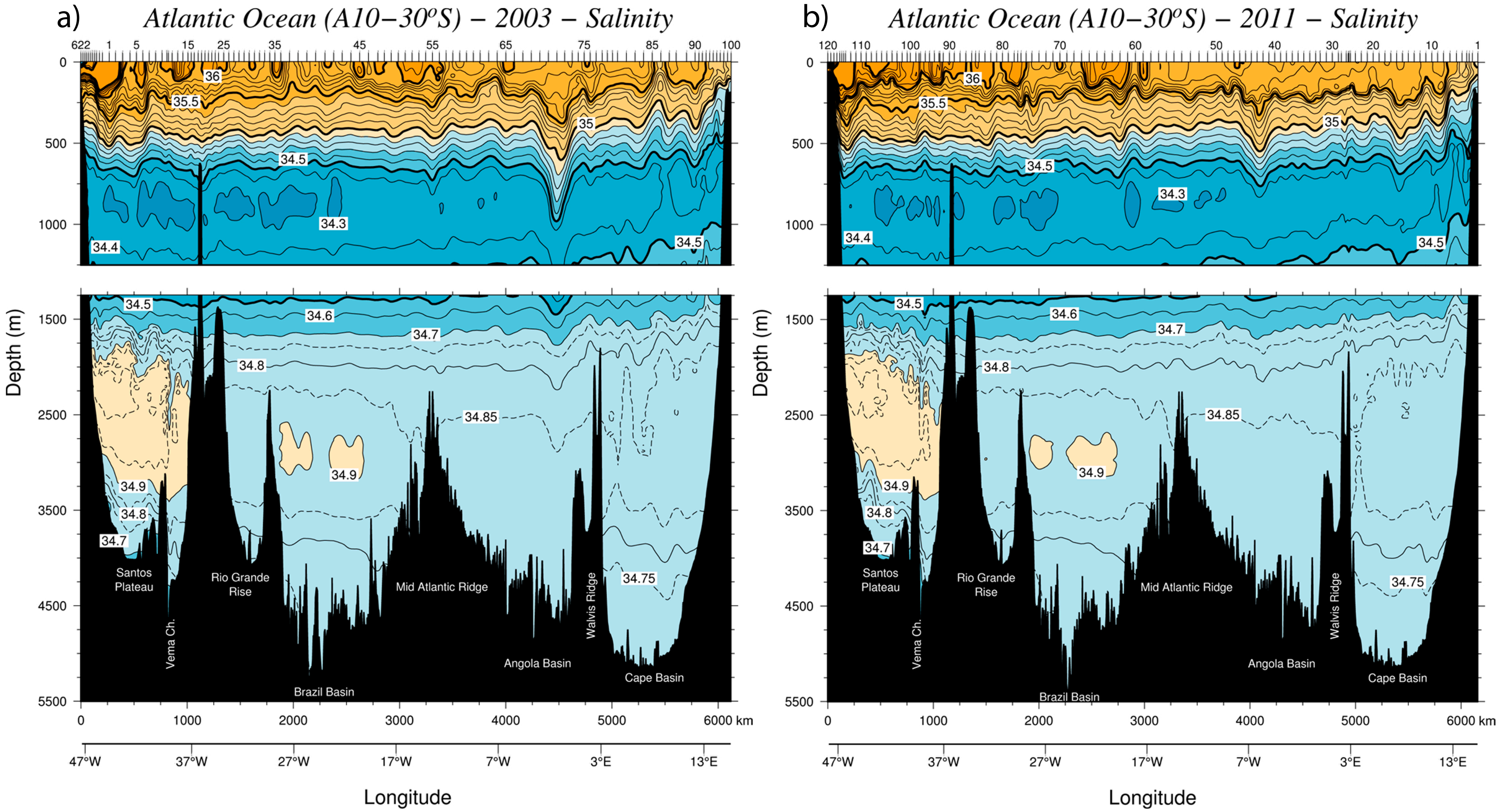
a)
Atlantic Ocean (A10–30°S) – 2003 – Salinity
b)
Atlantic Ocean (A10–30°S) – 2011 – Salinity
Depth (m)
0
500
1000
1500
2500
3500
4500
5500
36
35.5
35
34.5
34.4
34.3
34.6
34.7
34.8
34.85
34.9
34.75
Santos Plateau
Vema Ch.
Rio Grande Rise
Brazil Basin
Mid Atlantic Ridge
Angola Basin
Walvis Ridge
Cape Basin
0
1000
2000
3000
4000
5000
6000 km
47°W
37°W
27°W
17°W
7°W
3°E
13°E
Longitude

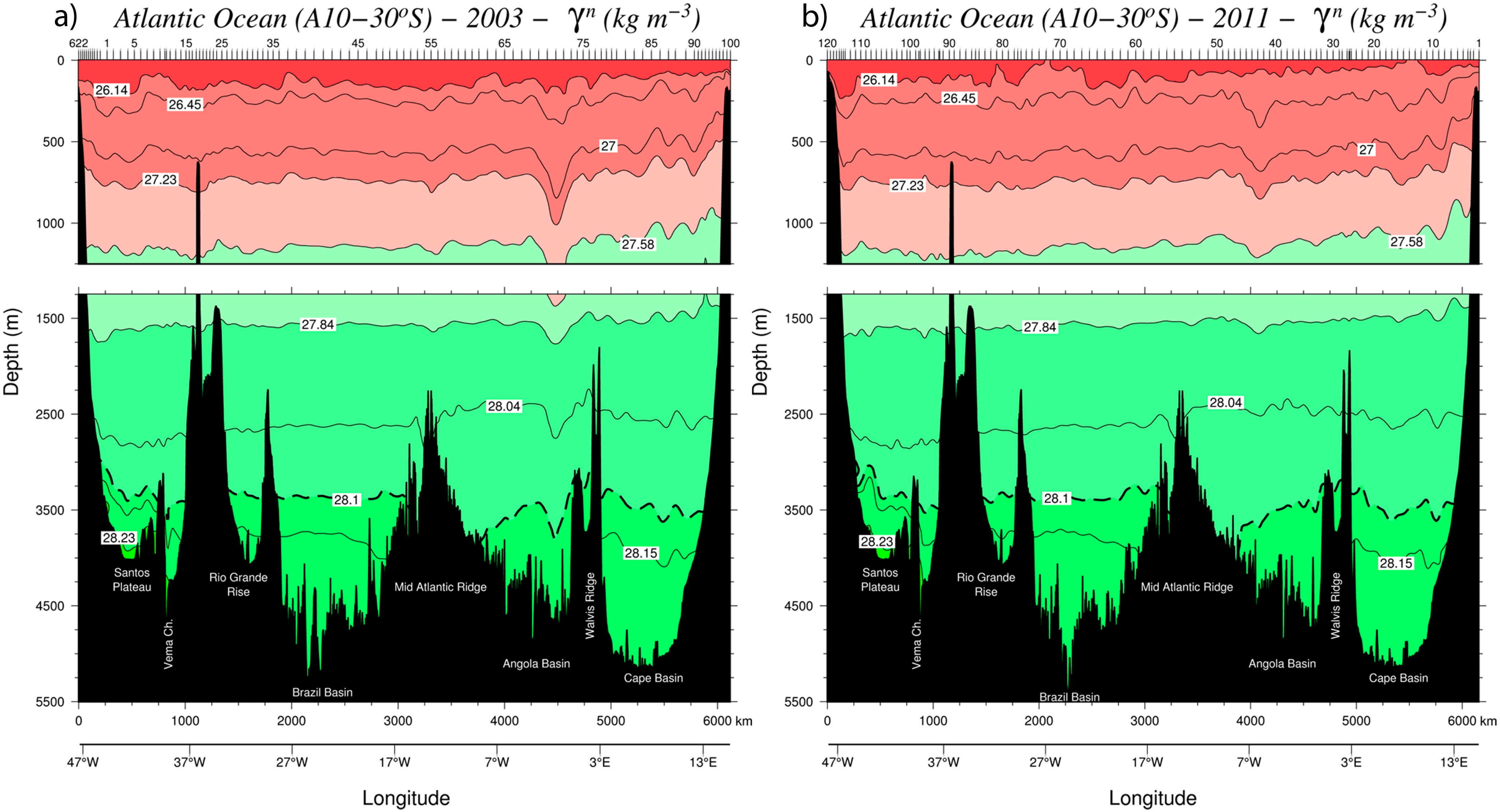
a)
Atlantic Ocean (A10–30°S) – 2003 – γⁿ (kg m⁻³)
b)
Atlantic Ocean (A10–30°S) – 2011 – γⁿ (kg m⁻³)
26.14
26.45
27
27.23
27.58
27.84
28.04
28.1
28.15
28.23
Santos Plateau
Vema Ch.
Rio Grande Rise
Brazil Basin
Mid Atlantic Ridge
Angola Basin
Walvis Ridge
Cape Basin
Depth (m)
0
500
1000
1500
2500
3500
4500
5500
0
1000
2000
3000
4000
5000
6000 km
47°W
37°W
27°W
17°W
7°W
3°E
13°E
Longitude

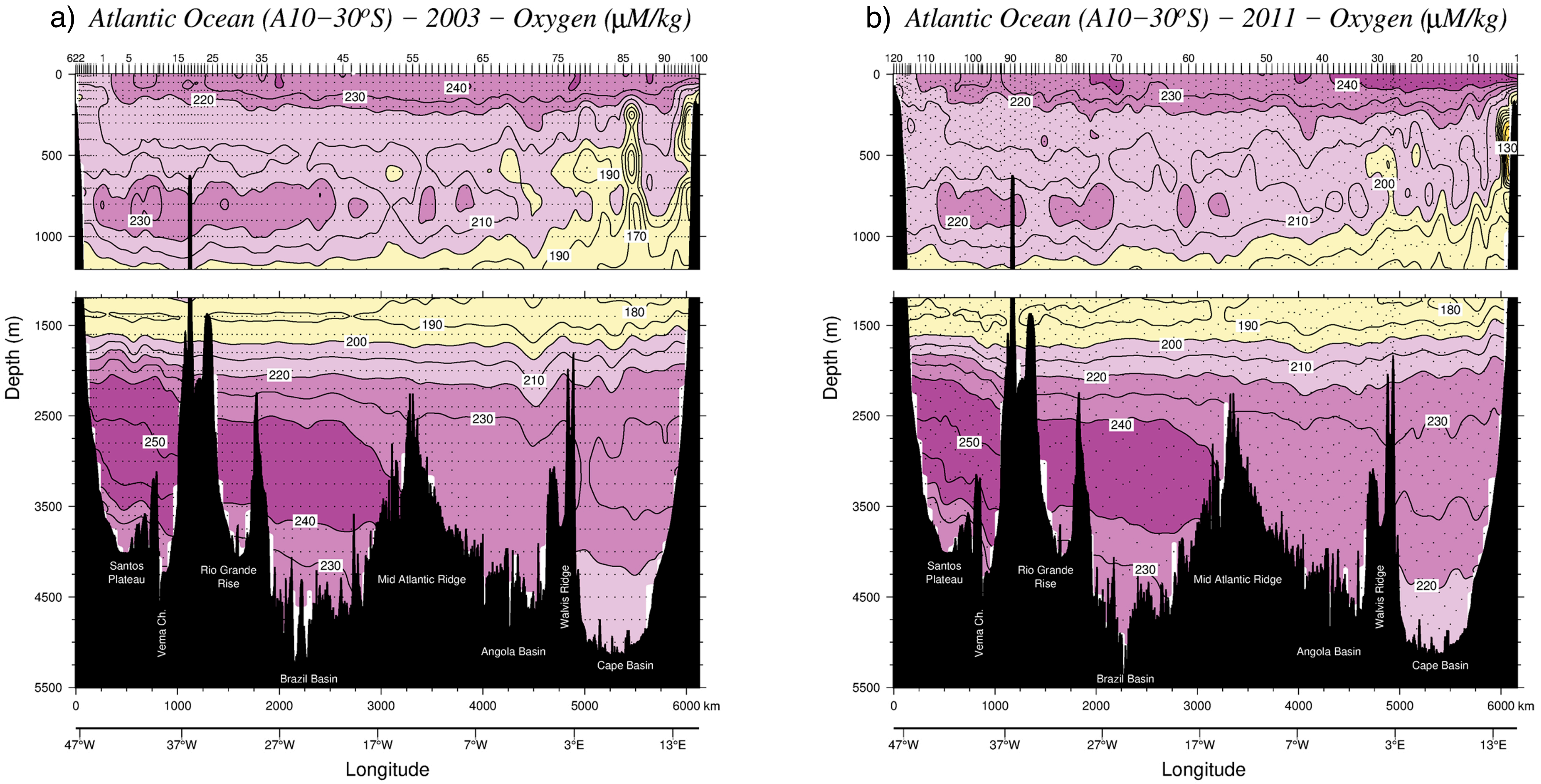

a) *Atlantic Ocean (A10−30ºS) − 2003 − Oxygen (μM/kg)*

b) *Atlantic Ocean (A10−30ºS) − 2011 − Oxygen (μM/kg)*

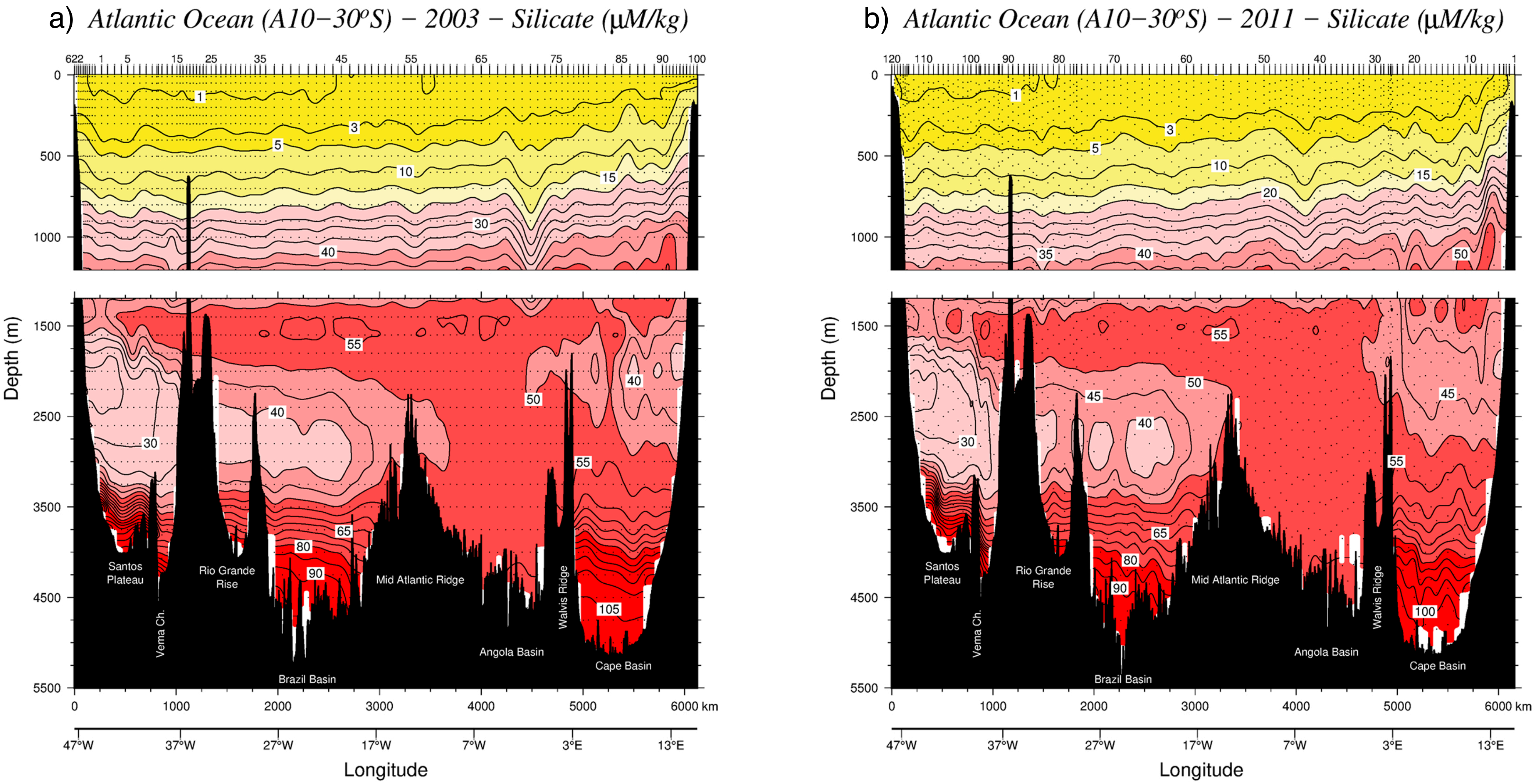
a) Atlantic Ocean (A10−30°S) − 2003 − Silicate (µM/kg)
b) Atlantic Ocean (A10−30°S) − 2011 − Silicate (µM/kg)
Depth (m)
0
500
1000
1500
2500
3500
4500
5500
0
1000
2000
3000
4000
5000
6000 km
47°W
37°W
27°W
17°W
7°W
3°E
13°E
Longitude
Santos Plateau
Vema Ch.
Rio Grande Rise
Brazil Basin
Mid Atlantic Ridge
Angola Basin
Walvis Ridge
Cape Basin
1
3
5
10
15
20
30
35
40
45
50
55
65
80
90
100
105

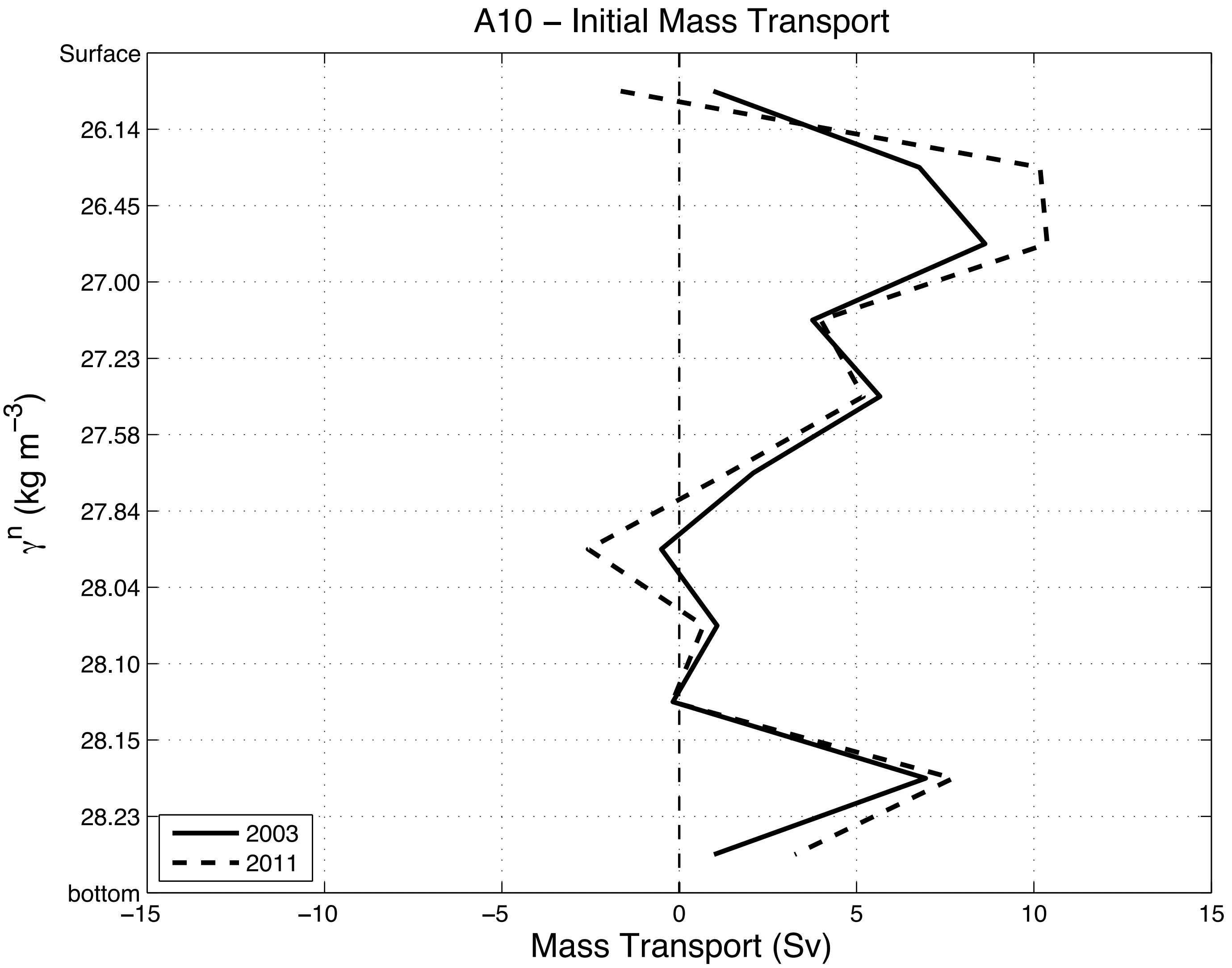

2003: 36.4 Sv

2011: 38.6 Sv

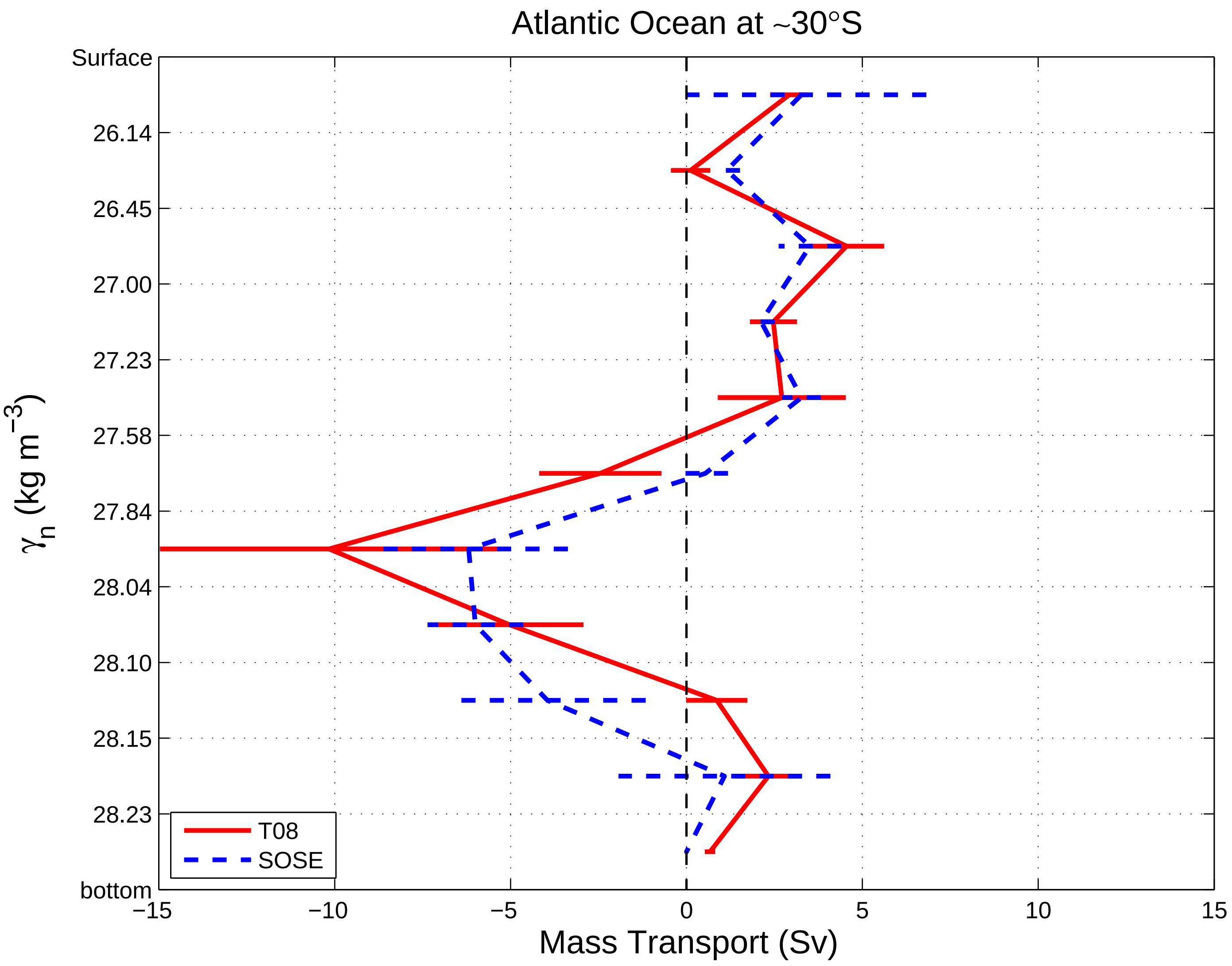
Atlantic Ocean at ~30°S
Surface
26.14
26.45
27.00
27.23
27.58
27.84
28.04
28.10
28.15
28.23
bottom
γ_n (kg m^{-3})
−15
−10
−5
0
5
10
15
Mass Transport (Sv)
T08
SOSE

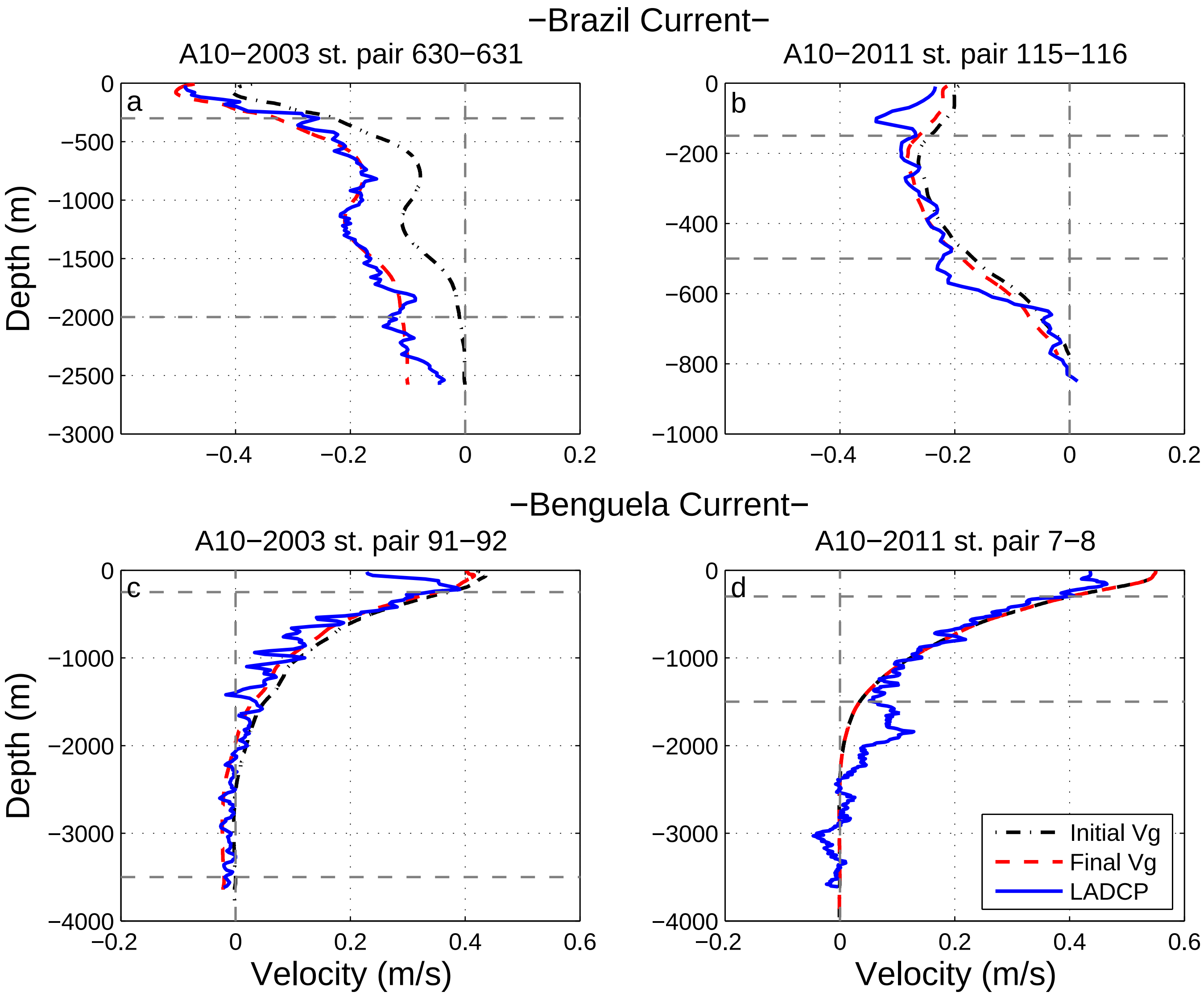
−Brazil Current−
A10−2003 st. pair 630−631
A10−2011 st. pair 115−116
a
b
Depth (m)
0
−500
−1000
−1500
−2000
−2500
−3000
−200
−400
−600
−800
−1000
−0.4
−0.2
0
0.2
−Benguela Current−
A10−2003 st. pair 91−92
A10−2011 st. pair 7−8
c
d
−4000
−0.2
0.4
0.6
Velocity (m/s)
Initial Vg
Final Vg
LADCP

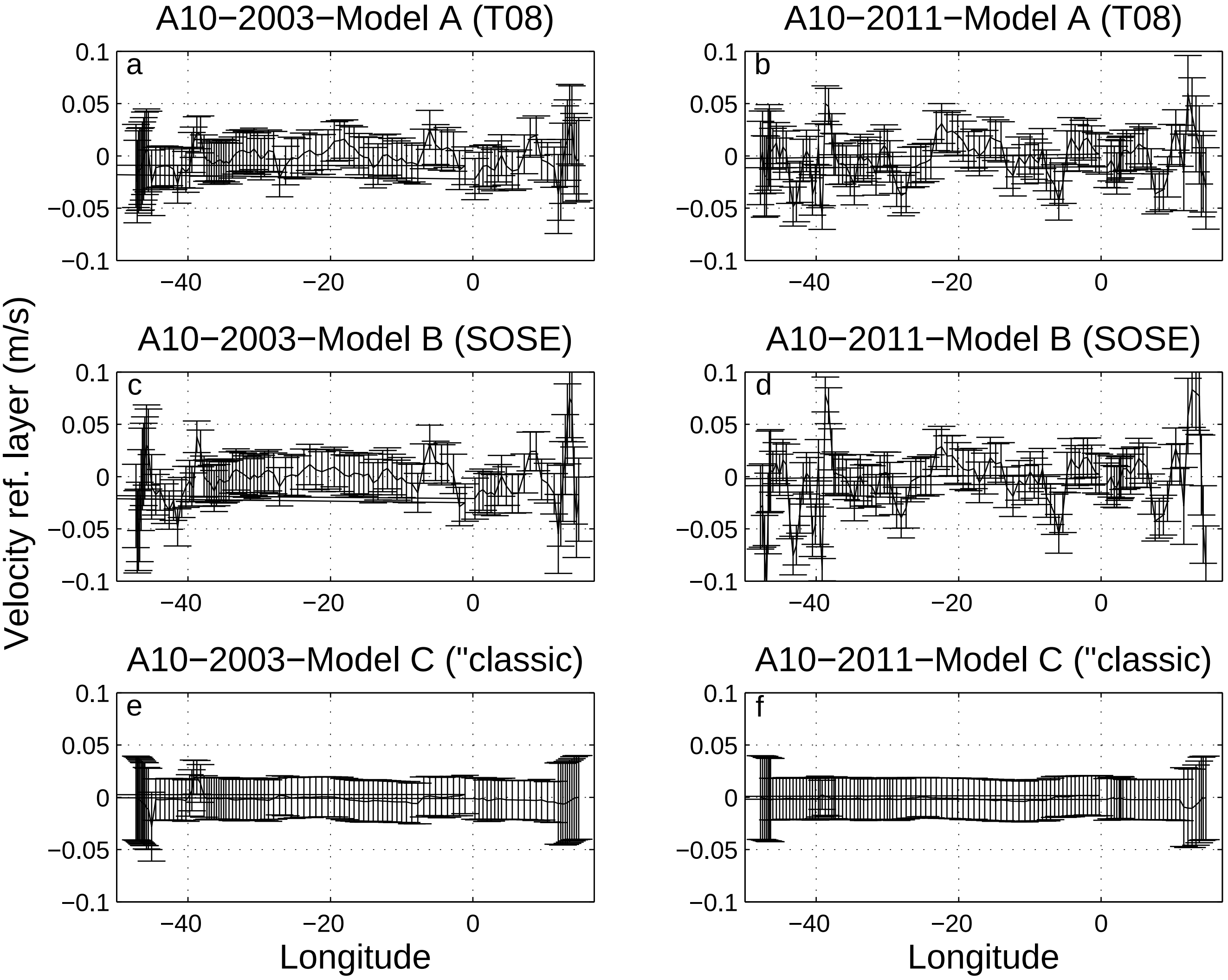
A10−2003−Model A (T08)
a
A10−2011−Model A (T08)
b
A10−2003−Model B (SOSE)
c
A10−2011−Model B (SOSE)
d
A10−2003−Model C ("classic)
e
A10−2011−Model C ("classic)
f
Velocity ref. layer (m/s)
0.1
0.05
0
−0.05
−0.1
−40
−20
0
Longitude

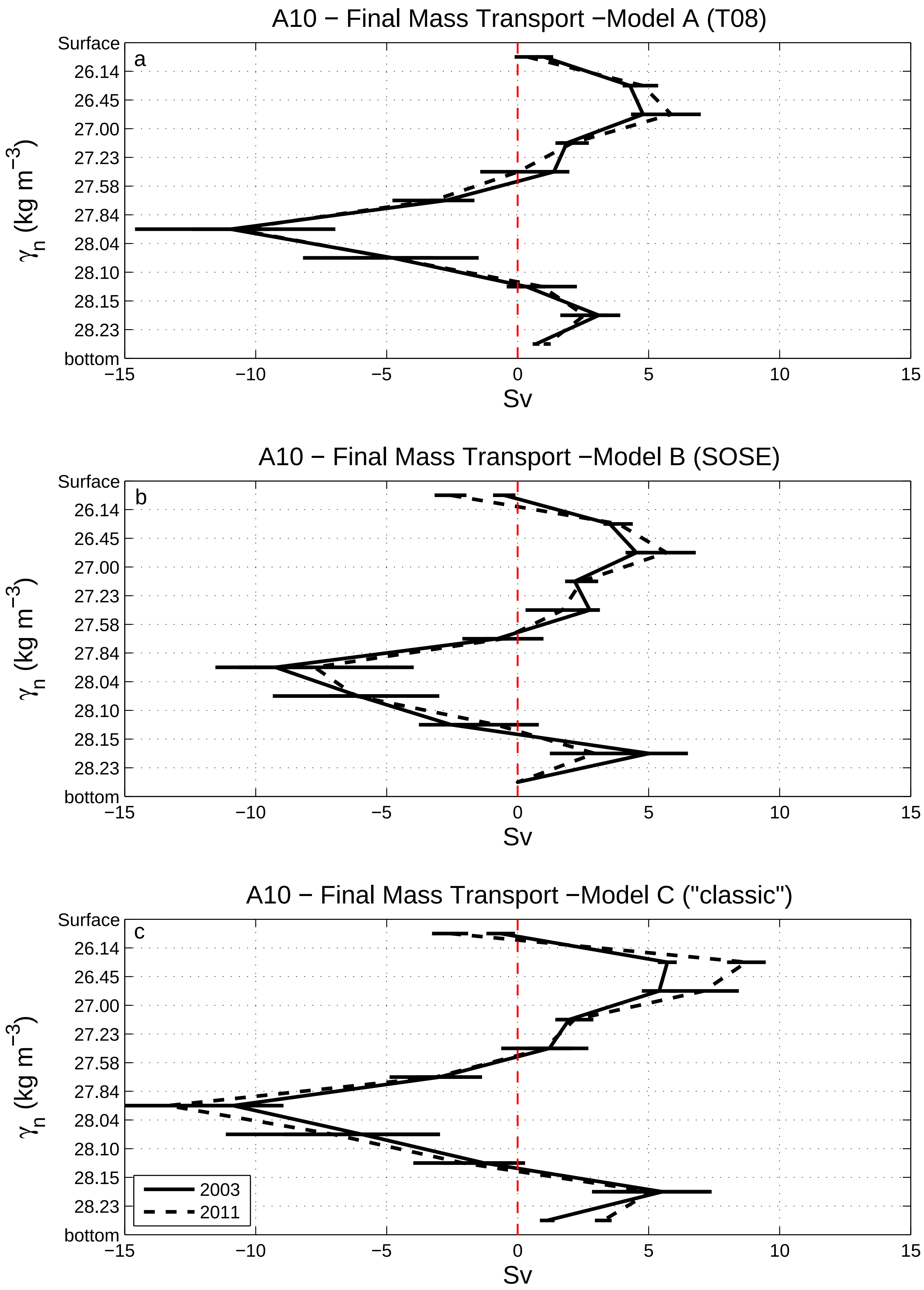
A10 − Final Mass Transport −Model A (T08)
a
Surface
26.14
26.45
27.00
27.23
27.58
27.84
28.04
28.10
28.15
28.23
bottom
γ_n (kg m^{-3})
−15
−10
−5
0
5
10
15
Sv
A10 − Final Mass Transport −Model B (SOSE)
b
Surface
26.14
26.45
27.00
27.23
27.58
27.84
28.04
28.10
28.15
28.23
bottom
γ_n (kg m^{-3})
−15
−10
−5
0
5
10
15
Sv
A10 − Final Mass Transport −Model C ("classic")
c
Surface
26.14
26.45
27.00
27.23
27.58
27.84
28.04
28.10
28.15
28.23
bottom
γ_n (kg m^{-3})
2003
2011
−15
−10
−5
0
5
10
15
Sv

A10 − Overturning Streamfunction − Model A (T08)

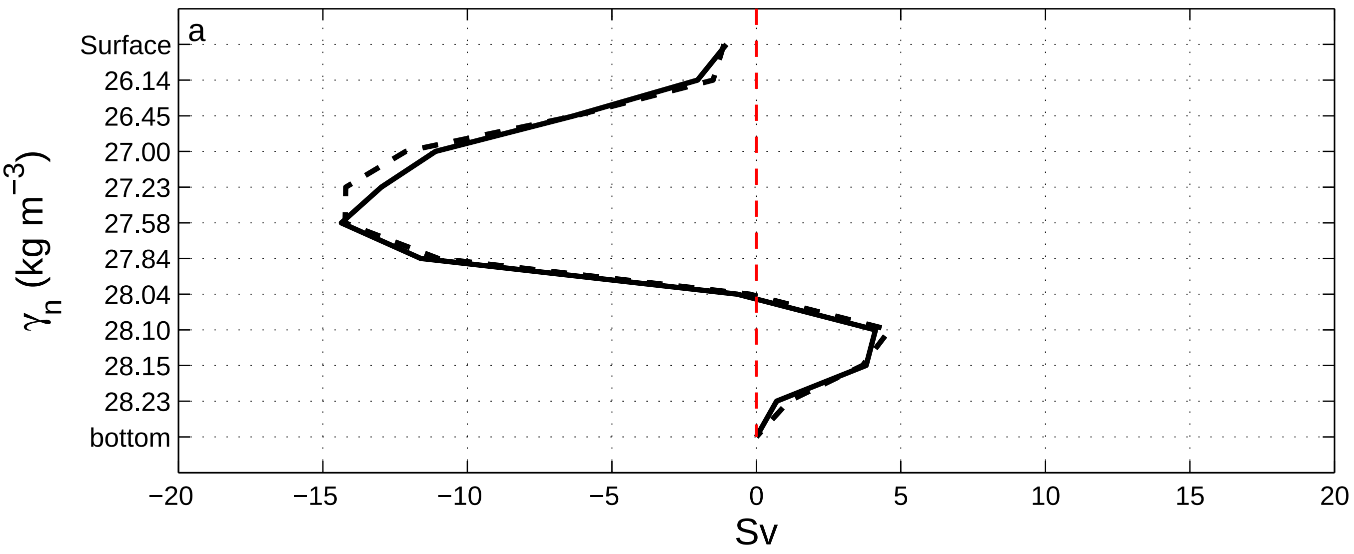

A10 − Overturning Streamfunction − Model B (SOSE)

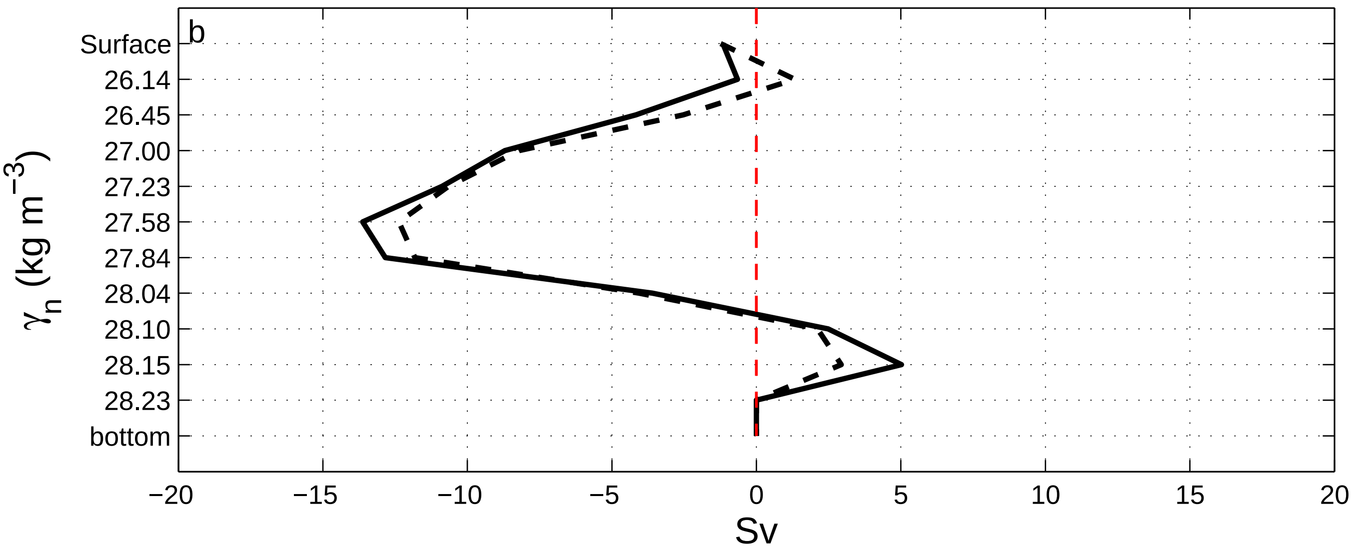

A10 − Overturning Streamfunction − Model C ("classic")

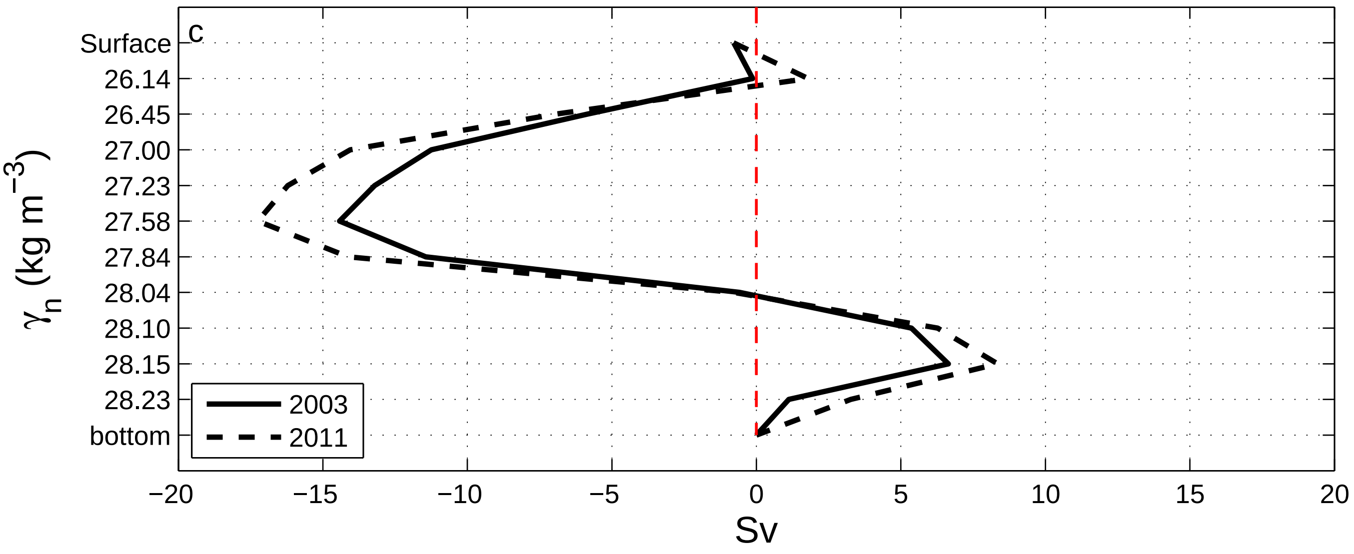

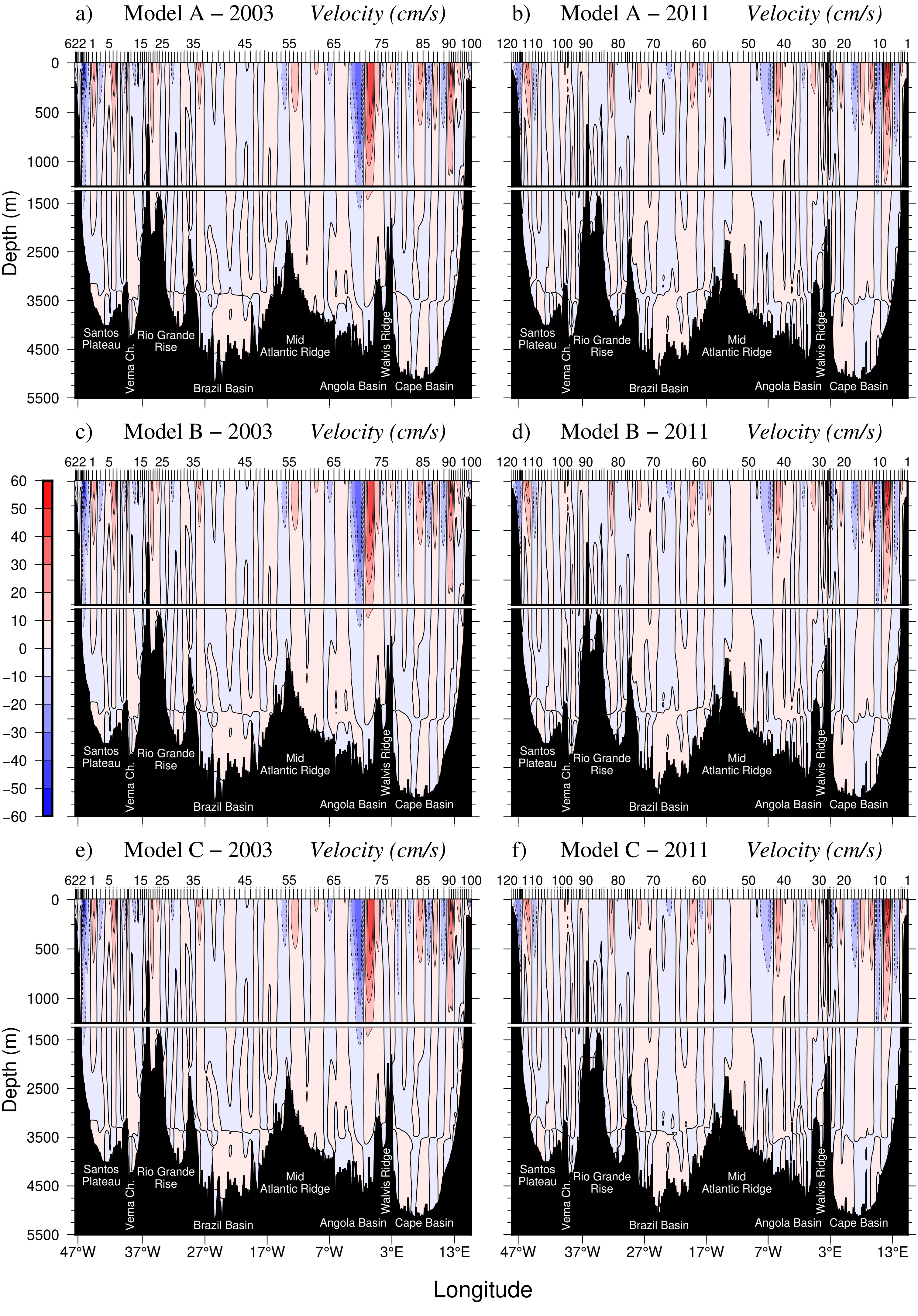
a) Model A – 2003 Velocity (cm/s)
b) Model A – 2011 Velocity (cm/s)
c) Model B – 2003 Velocity (cm/s)
d) Model B – 2011 Velocity (cm/s)
e) Model C – 2003 Velocity (cm/s)
f) Model C – 2011 Velocity (cm/s)
622 1 5 15 25 35 45 55 65 75 85 90 100
120 110 100 90 80 70 60 50 40 30 20 10 1
0
500
1000
1500
2500
3500
4500
5500
Depth (m)
Santos Plateau
Vema Ch.
Rio Grande Rise
Brazil Basin
Mid Atlantic Ridge
Angola Basin
Walvis Ridge
Cape Basin
60
50
40
30
20
10
0
−10
−20
−30
−40
−50
−60
47°W
37°W
27°W
17°W
7°W
3°E
13°E
Longitude

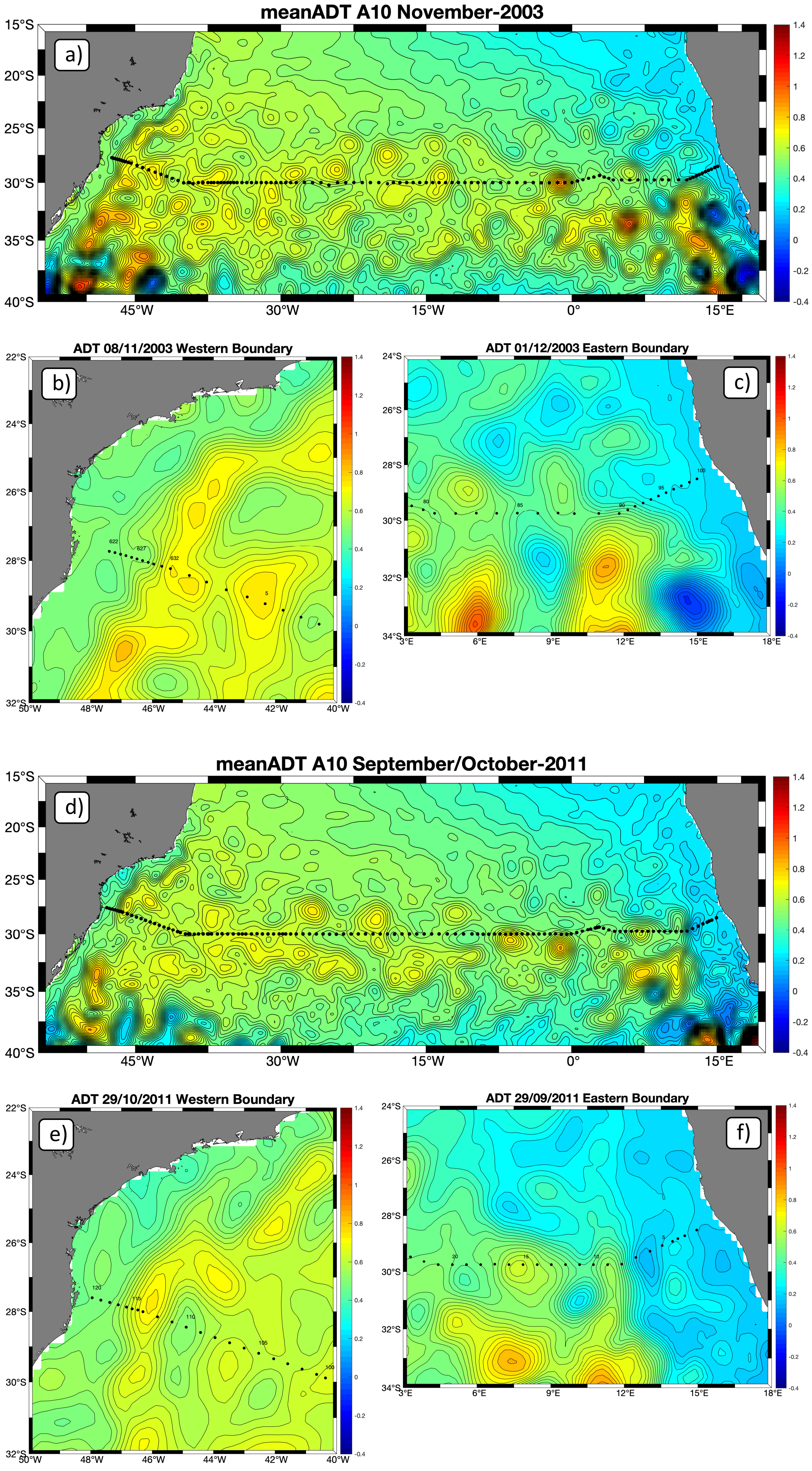meanADT A10 November-2003
a)
15°S
20°S
25°S
30°S
35°S
40°S
45°W
30°W
15°W
0°
15°E
1.4
1.2
1
0.8
0.6
0.4
0.2
0
-0.2
-0.4
ADT 08/11/2003 Western Boundary
b)
22°S
24°S
26°S
28°S
30°S
32°S
50°W
48°W
46°W
44°W
42°W
40°W
622
627
632
5
ADT 01/12/2003 Eastern Boundary
c)
24°S
26°S
28°S
30°S
32°S
34°S
3°E
6°E
9°E
12°E
15°E
18°E
80
85
90
95
100
meanADT A10 September/October-2011
d)
ADT 29/10/2011 Western Boundary
e)
120
115
110
105
100
ADT 29/09/2011 Eastern Boundary
f)
20
15
10
5

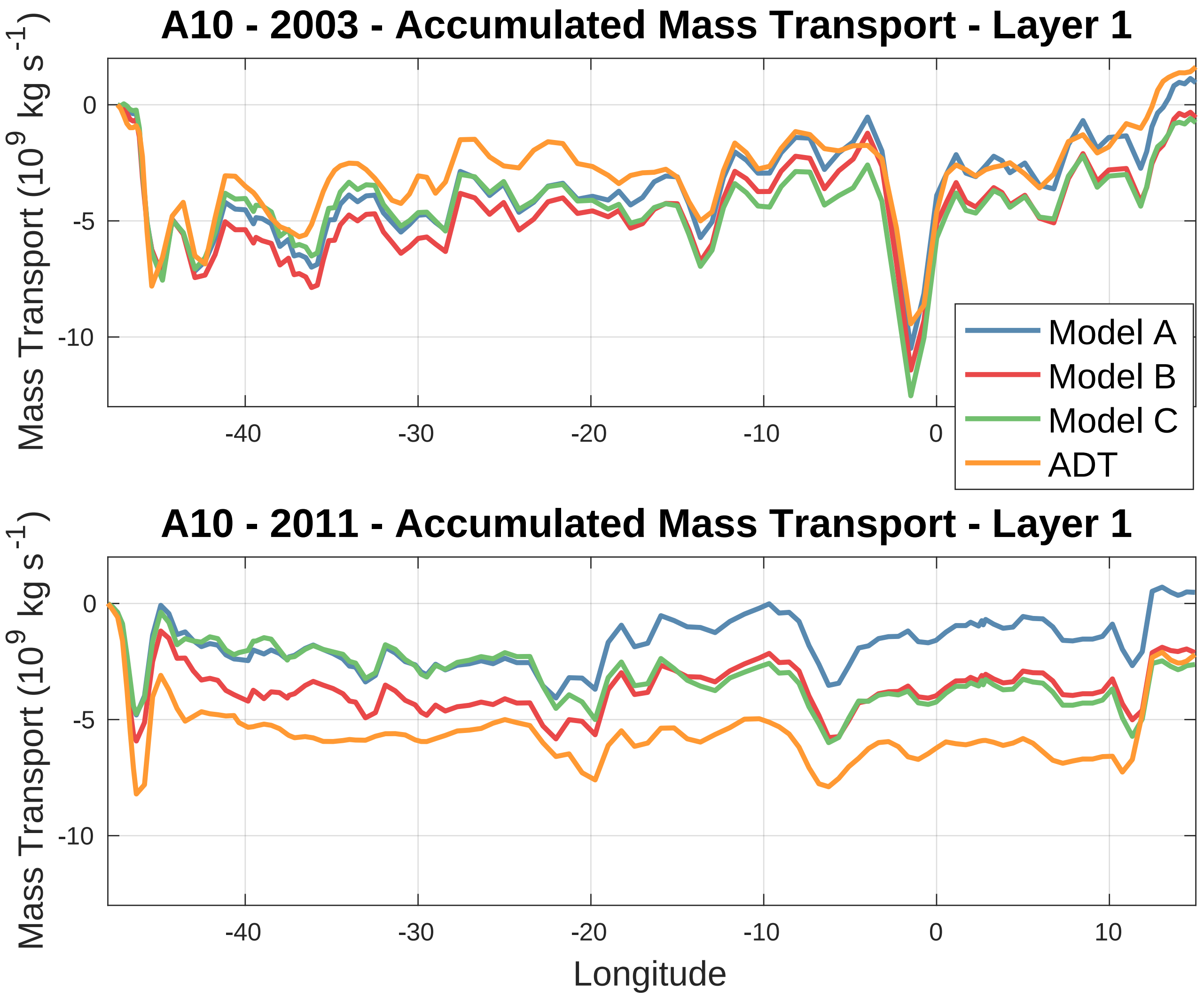
A10 - 2003 - Accumulated Mass Transport - Layer 1
A10 - 2011 - Accumulated Mass Transport - Layer 1
Mass Transport (10^9 kg s^{-1})
0
-5
-10
-40
-30
-20
-10
0
10
Longitude
Model A
Model B
Model C
ADT

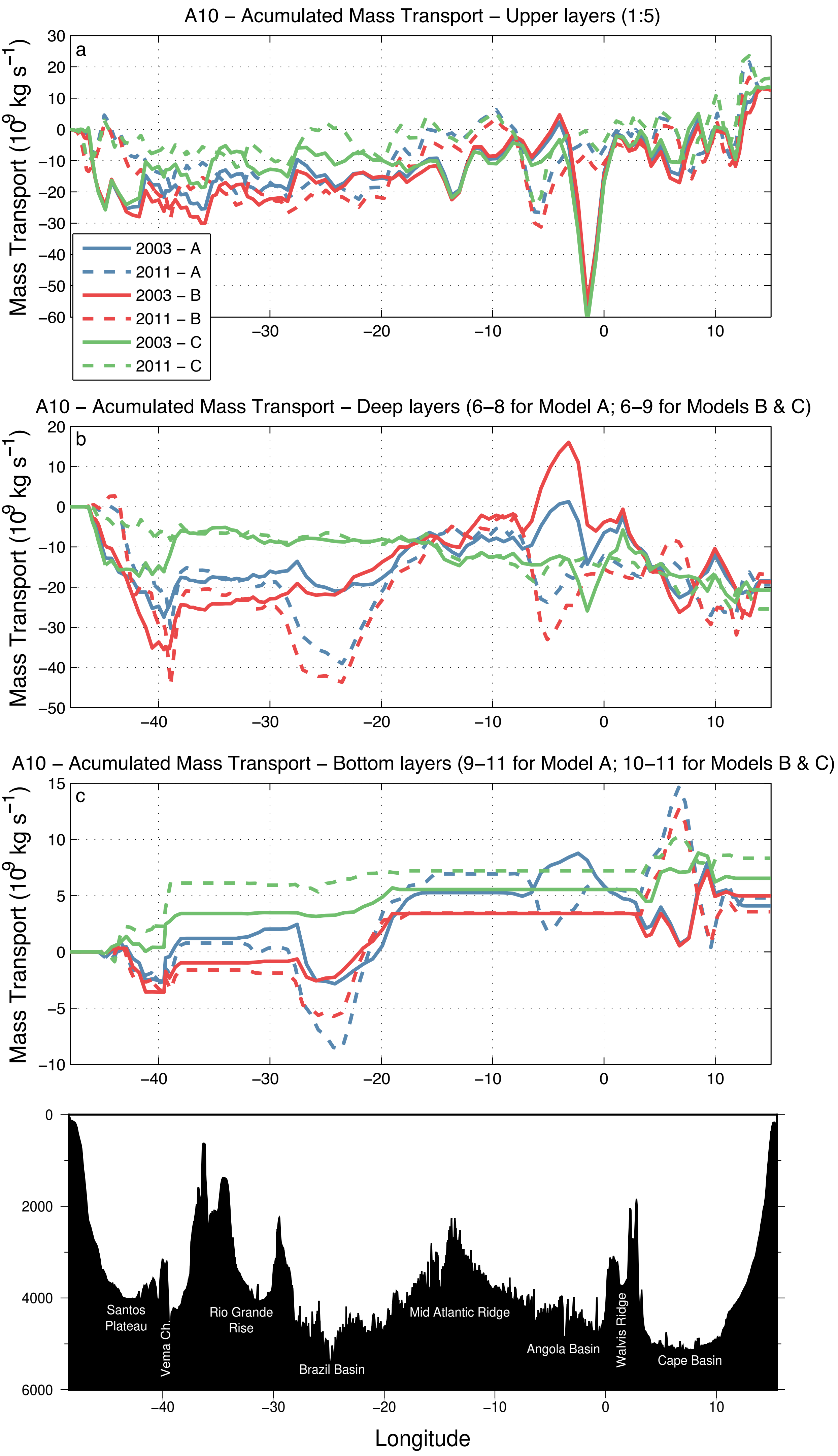

A10 – Acumulated Mass Transport – Upper layers (1:5)

A10 – Acumulated Mass Transport – Deep layers (6–8 for Model A; 6–9 for Models B & C)

A10 – Acumulated Mass Transport – Bottom layers (9–11 for Model A; 10–11 for Models B & C)

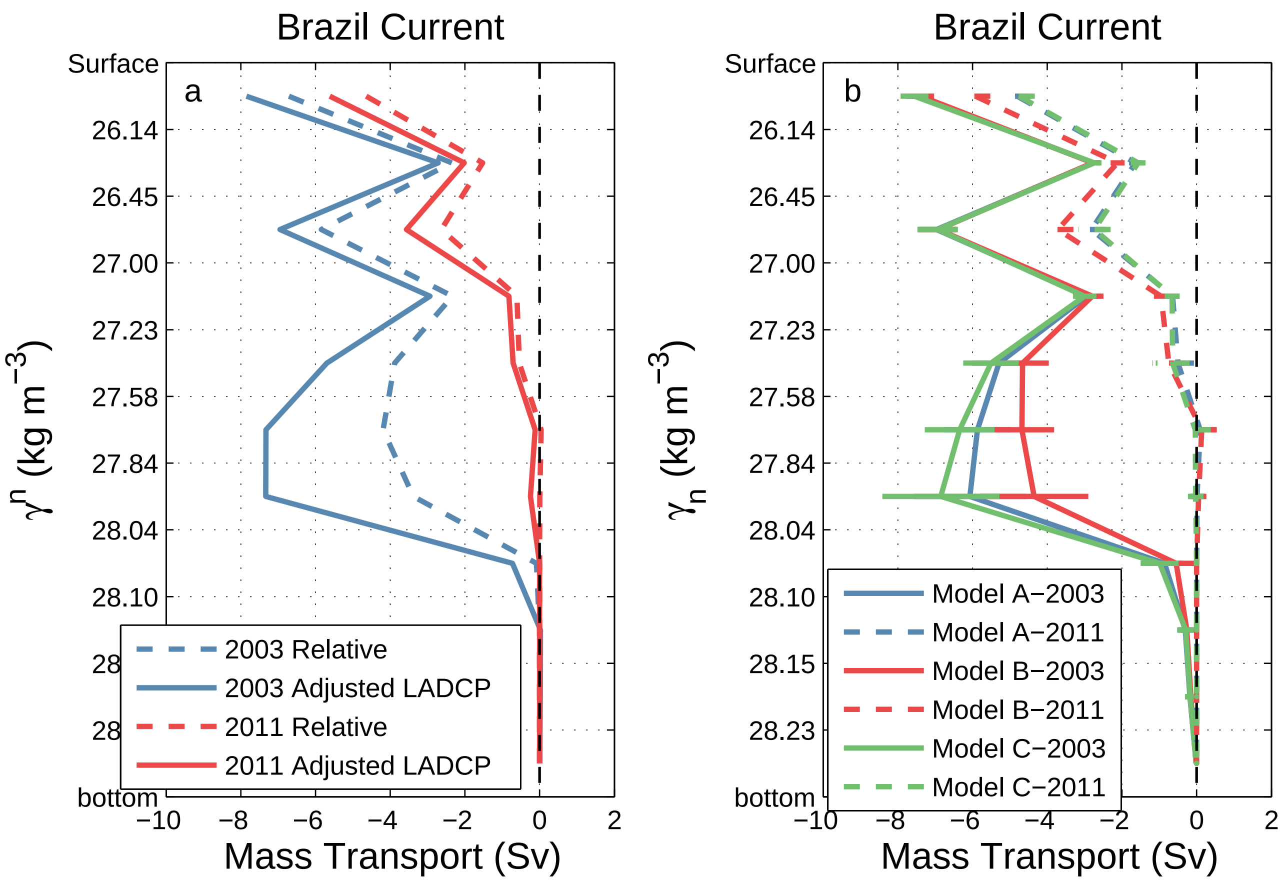
Brazil Current
Surface
a
26.14
26.45
27.00
27.23
27.58
27.84
28.04
28.10
28
28
bottom
γ^n (kg m^{-3})
−10
−8
−6
−4
−2
0
2
Mass Transport (Sv)
2003 Relative
2003 Adjusted LADCP
2011 Relative
2011 Adjusted LADCP
Brazil Current
Surface
b
26.14
26.45
27.00
27.23
27.58
27.84
28.04
28.10
28.15
28.23
bottom
γ_n (kg m^{-3})
−10
−8
−6
−4
−2
0
2
Mass Transport (Sv)
Model A−2003
Model A−2011
Model B−2003
Model B−2011
Model C−2003
Model C−2011